Hawley *et al.*
Acta Neuropathologica Communications (2025) 13:116
https://doi.org/10.1186/s40478-025-02005-z

Acta Neuropathologica
Communications

RESEARCH **Open Access**

Viral-mediated knockdown of *Atxn2* attenuates TDP-43 pathology and muscle dysfunction in the PFN1^{C71G} ALS mouse model

Zachary C. E. Hawley[1], Xueying Li[1], Dora Bodnar[1], Yuanzheng Gu[1], Yi Luo[1], Daniel Ferretti[1], Adam Sheehy[1], Rachelle Driscoll[1], Maria I. Zavodszky[1], Shaolong Cao[1], Isabel Isaza[1], Luke Jandreski[1], Yuqing Liu[1], Thomas Carlile[1], Shih-Ching Lo[1], Anna Grimard[1], Shawn Bourque[1], Aditya Utturkar[1], Samantha Desmarais[1], H. Moore Arnold[1], Dann Huh[1], Edward Guilmette[1] and Deborah Y. Kwon[1]*

Abstract

Amyotrophic lateral sclerosis (ALS) is a fatal neurodegenerative disorder characterized by progressive motor neuron loss and muscle atrophy. Hyperphosphorylated aggregation of the RNA-binding protein, TDP-43, in the motor cortex and spinal cord are defining molecular features of ALS, suggesting TDP-43 dysfunction underlies disease pathogenesis. This phenomenon, however, has been difficult to recapitulate endogenously in animal models, impeding characterization of TDP-43 pathobiology in neurodegeneration. In this study, we report age-dependent accumulation of TDP-43 pathology in the spinal cord and progressive muscle-related deficits in transgenic mice expressing the ALS-associated PFN1^{C71G} mutant protein. We show that transgenic neuronal expression of PFN1^{C71G} induces early hyperphosphorylation of endogenous TDP-43 in the spinal cord that augments over time, preceding accumulation of insoluble non-phosphorylated TDP-43 and the manifestation of muscle denervation and motor dysfunction. Sustained knockdown of Atxn2 in the central nervous system (CNS) in pre-symptomatic PFN1^{C71G} mice by AAV-driven expression of an artificial microRNA (AAV-amiR-Atxn2) reduces aberrant TDP-43 in the spinal cord, while delaying neurodegeneration and improving muscle and motor function. RNA-sequencing analysis of spinal cord samples from PFN1^{C71G} mice and ALS donors show shared patterns of transcriptional perturbation, including a pro-inflammatory gene signature that is attenuated by AAV-amiR-Atxn2. Notably, impaired regulation of the PFN1^{C71G} skeletal muscle transcriptome exceeds that of the spinal cord and is also improved by Atxn2 reduction in the CNS. Lastly, we find significant gene co-expression network homology between PFN1^{C71G} mice and human ALS, with shared dysregulation of modules related to neuroinflammation and neuronal function and uncover novel hub genes that provide biological insight into ALS and potential drug targets that can be further investigated in this mouse model.

Introduction

Amyotrophic lateral sclerosis (ALS) is a progressive motor neuron degenerative disease with a median survival of 2–3 years from symptom onset [1]. Ubiquitinated and hyperphosphorylated cytoplasmic inclusions of an essential nuclear protein, Tar DNA-binding protein of 43 kDa (TDP-43/T*ARDBP*), is a pathological hallmark of ALS occurring in ~ 97% of cases

---

*Correspondence:
Deborah Y. Kwon
deborahykwon@gmail.com
[1] Biogen, Cambridge, MA, USA

[2] and mutations in *TARDBP* have been discovered in ~ 3–5% of familial and ~ 1% of sporadic ALS cases [1]. This mis-localization and aggregation of TDP-43 results in both a cytoplasmic gain-of-function and a nuclear loss-of-function that is hypothesized to contribute to neuronal dysfunction and death [3–8]. Understanding when and how TDP-43 pathology begins to develop using the appropriate model systems is essential to develop effective therapeutics targeting TDP-43 dysregulation in ALS.

In vivo TDP-43 overexpression models have been largely used to assess potential therapeutics that address TDP-43 gain-of-function toxicities. One such model is the TAR4/4 mouse model, which overexpresses human TDP-43 and recapitulates many ALS-associated phenotypes, including phosphorylated TDP-43 inclusions in the cytoplasm and progressive motor neuron degeneration [9]. Downregulation of *Ataxin-2* (*Atxn2*), an ALS-associated gene, in TAR4/4 mice proved effective in mitigating TDP-43 pathology and disease progression, which suggested Atxn2 reduction could be effective at attenuating TDP-43 related toxicities in ALS [10–13]. However, in ALS, TDP-43 is not overexpressed, and reliance on TDP-43 overexpression models may confound mechanistic and therapeutic discovery. Indeed, a recent report found that TDP-43 overexpression induces species-specific exon skipping events that are irrelevant to ALS biology, underscoring the importance of assessing whether the pathological changes in these overexpression models are translatable to ALS [14]. Thus, non-TDP-43 overexpressing models that replicate the disease pathophysiology are necessary for the development of TDP-43-pathology-targeting therapies.

Profilin 1 (PFN1) is a ubiquitously expressed protein regulating actin and microtubule dynamics and is essential for proper cytoskeleton formation, with particular relevance for neurons possessing long axonal tracts [15]. ALS-causative mutations in PFN1 induce a loss-of-function, impacting the protein's ability to bind either actin and/or microtubules [16, 17]. Several of the mutations, most notably C71G, also reduce PFN1 solubility, causing it to form toxic insoluble aggregates [16]. Interestingly, in vitro overexpression of ALS-relevant PFN1 mutants, including PFN1^{C71G}, can sequester TDP-43 into cytoplasmic inclusions, resulting in TDP-43 phosphorylation, and mutant PFN1 can exacerbate TDP-43 pathology in *Drosophila melanogaster* models overexpressing TDP-43 [18–20]. Additionally, histopathology of a subgroup of people with ALS that harbor rare mutations in PFN1 show TDP-43 cytoplasmic inclusions in both spinal motor neurons and glial cells [21]. Collectively, these data suggest PFN1 dysregulation through ALS-causing mutations promotes TDP-43 pathology.

Previously, Yang et al., developed a triple transgenic mouse model that exogenously expresses the human PFN1 gene harboring the C71G ALS-related mutation [22]. These animals are homozygous for the Thy1.2-V5-PFN1^{C71G} transgenic allele and hemizygous carriers of the Prp-V5-PFN1^{C71G} transgenic allele that are expressed in neuronal cells of the CNS, including spinal motor neurons [22]. This model replicated many of the characteristics associated with ALS including progressive motor neuron and axonal degeneration, neuromuscular junction denervation, and muscle atrophy with concomitant motor deficits and eventual paralysis. Furthermore, histopathology of PFN1^{C71G} mice revealed PFN1 cytoplasmic inclusions that were ubiquitin and p62 positive in spinal motor neurons [22]. While this model displays several features of ALS, whether it also develops disease-inducing TDP-43 pathology and is translatable to human disease have yet to be determined.

Here, we provide a comprehensive characterization of the PFN1^{C71G} triple transgenic model, developing timelines of disease progression through behavioral, pathological, and biochemical analyses. We identify early accumulation of insoluble phosphorylated TDP-43 within the spinal cord of PFN1^{C71G} mice—reminiscent of the pathology observed in broad ALS—prior to the development of neurodegeneration, muscle atrophy and motor deficits. Furthermore, reduction of Atxn2 at the onset of TDP-43 hyperphosphorylation, via an adeno-associated virus (AAV) delivered artificial miRNA (AAV-amiR-Atxn2) in the CNS, reduces the accumulation of insoluble TDP-43 in the spinal cord and delays disease progression without altering PFN1^{C71G} pathology. This study provides the first evidence that TDP-43 pathology development induces disease without transgenic overexpression of TDP-43, and that modification of TDP-43 pathology through Atxn2 targeting can also be beneficial in a non-TDP-43-overexpression model of ALS. Through RNA-sequencing, we find molecular programs dysregulated in PFN1^{C71G} mouse spinal cord have human disease relevance, being observed in the spinal cord of post-mortem sporadic, C9orf72 and SOD1 ALS donors. Importantly, our study uncovers acute transcriptional dysregulation in skeletal muscle tissues of PFN1^{C71G} mice that exceeds the spinal cord, including a robust inflammation-related gene signature that is partially recovered by AAV-amiR-Atxn2. Together, these findings demonstrate the translatability of the PFN1^{C71G} mouse model to assess therapeutics for broad ALS and feature muscle as a potential source of insight into ALS pathophysiology and disease progression.

Results

Hemi/hom PFN1^{C71G} mice show neuromuscular junction (NMJ) denervation before significant loss of lower motor neurons

To develop a detailed understanding of the cascade of neurodegenerative events that transpire in the PFN1^{C71G} triple transgenic mice, we first characterized the histopathological consequences of sustained neuronal overexpression of PFN1^{C71G} in the ALS-relevant motor cortex, spinal cord, and skeletal muscle tissues. Triple transgenic PFN1^{C71G} mice (Prp-V5-PFN1^{C71G} hemizygous, Thy1.2-V5-PFN1^{C71G} homozygous; Fig. S1A), heretofore referred as Hemi/Hom, were previously reported as developing ALS-like motor phenotypes significantly earlier and more rapidly than single transgenic mice expressing one Thy1.2-V5-PFN1^{C71G} allele (referred to as WT/Hemi; Fig. S1A). We aged Hemi/Hom mice (n = 6) for 28 weeks until each animal displayed bilateral hindlimb clasping, an indicator of hindlimb muscle weakness and neurodegeneration, and used age-matched asymptomatic WT/Hemi littermates (n = 6) as controls (Fig. 1A). Consistent with the number of transgenic alleles expressed, we observed increased V5-tagged PFN1^{C71G} expression in Hemi/Hom mouse cortex (Fig.S1B, L) and spinal cord (Fig. S1E, L) relative to WT/Hemi mice; however, signs of neurodegeneration in Hemi/Hom mice were observed exclusively in the spinal cord at this symptomatic timepoint (Fig. 1B), with a trend towards a reduction in motor neurons in the lumbar spinal cord and no obvious histopathological signs of neuronal loss in the motor cortex (Fig. S1B, C).

We next looked further distally to neuromuscular junction (NMJ) terminals in skeletal muscle. The vast majority of NMJs in the gastrocnemius muscles of WT/Hemi mice showed full co-localization of presynaptic nerve staining and postsynaptic acetylcholine clustering, representing fully innervated NMJ terminals. In contrast, Hemi/Hom mice showed a roughly 65% reduction in fully innervated terminals (Fig. 1C,D) and a ~ 17% reduction in motor endplate area (Fig. 1E) relative to WT/Hemi controls. Given the marked NMJ pathology, we examined muscle fiber histology of the gastrocnemius muscle in the same symptomatic Hemi/Hom animals. Significant widespread muscle atrophy was observed in Hemi/Hom mice (Fig. 1F), with a 42% drop in lesser muscle fiber diameter (Fig. 1G) and a shift in muscle fiber size distribution from a peak of approximately 40 µm in WT/Hemi mice to 15 µm in Hemi/Hom samples (Fig. 1H). Compound muscle action potentials (CMAP) were also measured as orthogonal validation of NMJ dysfunction. CMAP provides the functional status of a motor unit pool by measuring the electrophysiological output of a selected group of muscles following supramaximal stimulation of peripheral nerve. We found that neurotransmission in the TA was impacted with age, with Hemi/Hom mice showing reduced CMAP amplitudes at the symptomatic 28-week-old mice but not at 12 weeks of age (Fig. 1l).

Together, these data indicate that triple transgenic PFN1^{C71G} mice display a 'dying back' degeneration of lower motor neurons over time, with the largest impact of sustained overexpression of PFN1^{C71G} localized to the NMJ and skeletal muscle.

Increased insoluble pTDP-43 and TDP-43 observed in spinal cord tissues of phenotypic hemi/hom PFN1^{C71G} mice

Accumulation of insoluble phosphorylated TDP-43 (pTDP-43) and TDP-43 protein are pathological hallmarks of ALS, but few mouse models of ALS have been shown to recapitulate this feature. We asked whether phenotypic PFN1^{C71G} mice also developed TDP-43 pathology. Cortical and spinal cord tissues from 28-week-old WT/Hemi and Hemi/Hom mice were processed for immunoblotting and pTDP-43 at the disease-relevant S409/410 site and TDP-43 proteins were assayed in the NP-40 soluble and NP-40 insoluble (urea soluble) protein fractions. pTDP-43 protein was undetectable in the cortex of either WT/Hemi and Hemi/Hom mice. Likewise, TDP-43 was comparably expressed between the two genotypes, consistent with the lack of histological findings in the cortex (Fig. S1D).

In contrast, pTDP-43 was detected in the insoluble, but not soluble, protein fractions of both WT/Hemi and Hemi/Hom spinal cord samples, with a significant 48.1% increase in symptomatic Hemi/Hom mice relative to WT/Hemi mice (Fig. 1J, K). A more modest, yet significant 38.1% increase in TDP-43 was also observed in the insoluble, but not soluble, protein fraction of Hemi/Hom mice relative to WT/Hemi controls (Fig. 1J, L, M). These observations indicate the presence of TDP-43 pathology in spinal cords of mice exhibiting motor neuron degeneration and muscle denervation.

Progressive neurodegeneration and muscle dysfunction in hemi/hom PFN1^{C71G} mice

Having confirmed lower motor neuron pathology in symptomatic Hemi/Hom PFN1^{C71G} mice with concomitant TDP-43 proteinopathy, we next sought to determine the sequence of these neurodegenerative events by examining the onset of TDP-43 pathology, motor neuron degeneration, muscle dysfunction, and motor deficits. We first performed a battery of motor function tests on Hemi/Hom animals and age-matched WT/Hemi controls to quantify the progression of neuromuscular weakness

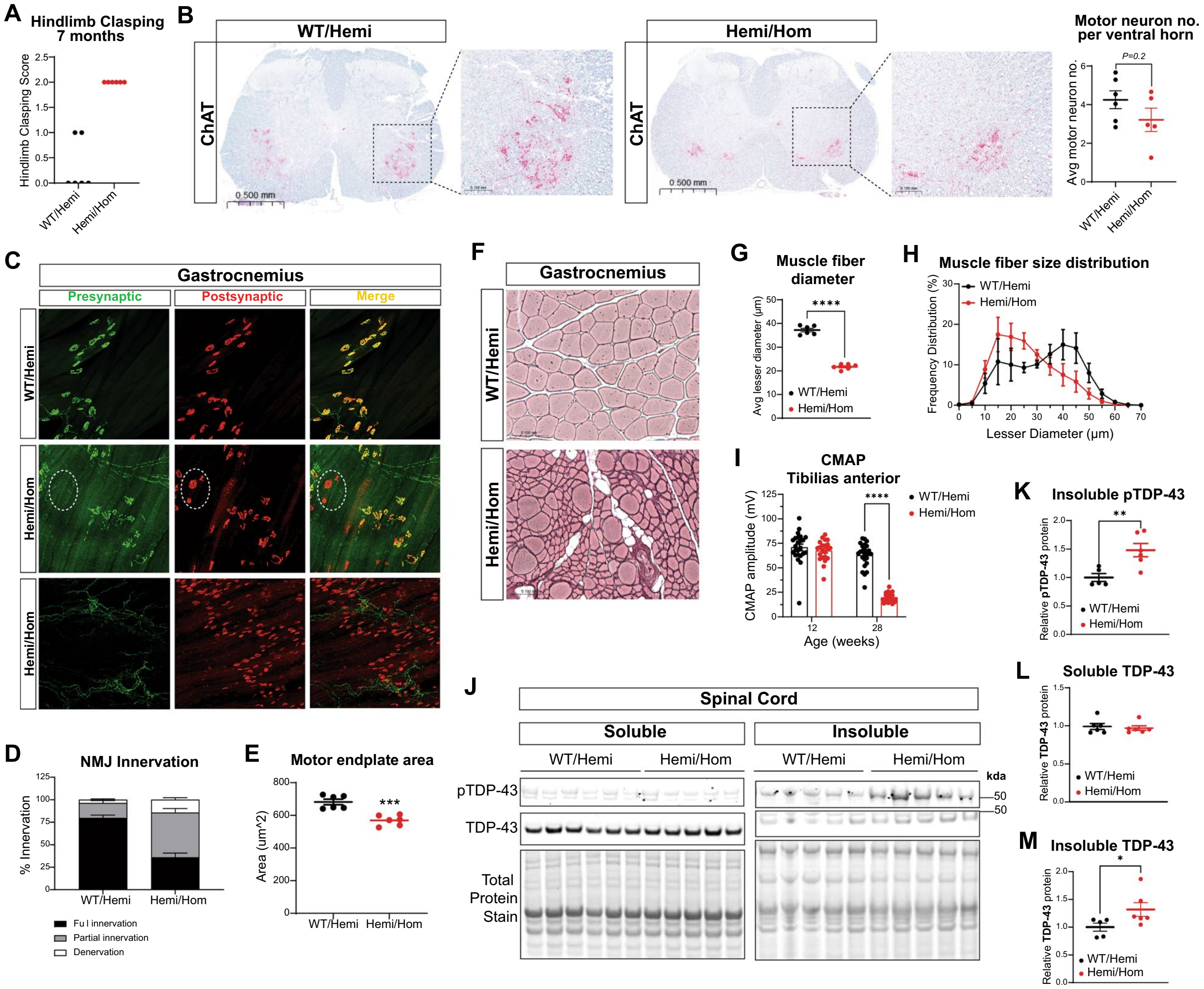

Fig. 1 Symptomatic Hemi/Hom PFN1^{C71G} transgenic mice show significant TDP-43 pathology and muscle denervation without commensurate loss of spinal motor neurons. **A** Hindlimb clasping scores in 28-week-old WT/Hemi and Hemi/Hom PFN1^{C71G} transgenic mice. A score of 2 represents clasping of both hindlimbs. **B** Representative immunohistology images of ChAT + motor neurons in lumbar spinal cord sections of PFN1^{C71G} WT/Hemi and Hemi/Hom mice (left). Quantification of motor neuron number per ventral horn (right) showing a trend towards reduced motor neuron number in Hemi/Hom (n = 6) mice (Unpaired t-test). **C** Representative images of NMJs in gastrocnemius muscles of WT/Hemi and Hemi/Hom mice stained with presynaptic neurofilament/SV2 (green) and post-synaptic bungarotoxin (red). White dotted ellipse encircles a cluster of denervated NMJ terminals in one Hemi/Hom animal and bottom images from another Hemi/Hom mouse show widespread muscle denervation. **D** Quantification of NMJ innervation status and **E** motor endplate area in WT/Hemi and Hemi/Hom animals (Unpaired t-test). **F** Representative histological images of reticulin-stained gastrocnemius muscles from WT/Hemi and Hemi/Hom animals. **G** Quantification of average gastrocnemius muscle fiber diameter (Unpaired t-test) and **H** size distribution. **I** CMAP amplitudes decline with age in Hemi/Hom mice (2-way ANOVA with Sidak's multiple comparisons). **J** Representative western blots showing phosphorylated TDP-43 (pTDP-43), TDP-43, and total protein levels in NP-40 soluble and insoluble (urea soluble) protein fractions from WT/Hemi and Hemi/Hom spinal cord tissues. Semi-quantification of **K** insoluble pTDP-43 (Unpaired t-test), **L** soluble TDP-43 (Mann–Whitney U-test), and **M** insoluble TDP-43 protein (Mann–Whitney U-test). For all graphs, each point denotes an individual subject (WT/Hemi, n = 6; Hemi/Hom, n = 6). Error bars represent s.e.m. and statistical tests were two-sided unless stated otherwise. **P < 0.05; **P < 0.01; ***P < 0.001; ****P < 0.0001*

over time. A consistent reduction in locomotion in an open field arena was observed in Hemi/Hom mice at all timepoints tested (Fig. 2A) while rearing duration—vertical behavior requiring hindlimb strength—was initially comparable between genotypes but decreased more rapidly in Hemi/Hom animals, with significant diminishment observed by 24 weeks of age (Fig. 2B). Similarly, grip strength (Fig. 2C) and rotarod performance (Fig. 2D) in Hemi/Hom mice also began to decline at approximately 20 weeks of age with statistical significance from WT/

Hemi controls achieved by 24 weeks of age. Hindlimb clasping also steadily progressed in Hemi/Hom mice over time; clasping of both hindlimbs was seen by 28 weeks of age (Fig. 2E), as previously observed (Fig. 1A).

The principal function of skeletal muscle is to generate force and reduced force is a key physiological consequence of muscle disorders. To determine if the observed motor deficits in Hemi/Hom PFN1^{C71G} mice correlated with impaired muscle function and neurodegeneration, muscle force in the gastrocnemius (GA) and CMAP amplitude in the tibialis anterior (TA) were measured monthly beginning at 8 weeks of age, approximately the earliest timepoint that electrophysiological measurements could be consistently recorded. Maximum muscle specific force, recorded using the dual-mode lever assay, was generated by GA plantar flexor force by tibialis nerve stimulation. Muscle specific force decreased from baseline by 16 weeks of age and significantly at 20 weeks of age (Fig. 2G), even after normalizing the absolute force to the GA muscle weight, which also waned over time (Fig. 2F). Muscle force-frequency relation, where gradually increasing stimulation frequencies are applied to achieve full complete tetanus, also changed with age; GA in 24-week-old Hemi/Hom mice produced significantly lower muscle force (Fig. S1F). When normalized to baseline, trending leftward shifts in muscle-force frequency was observed over time in Hemi/Hom mice at lower stimulation frequencies (Fig. S1G), suggesting progressive impairment in skeletal muscle contractile properties. The sciatic nerve motor axons innervating the tibialis anterior muscle were also altered in Hemi/Hom mice—CMAP amplitudes declined significantly by 16 weeks of age from baseline and continued to diminish over time (Fig. 2H). Latency to first CMAP peak from stimulation was largely consistent across all timepoints tested, suggesting impairment in axon myelination and initiation to CMAP depolarization does not underlie the observed deficits in NMJ transmission (Fig. S1H, I). Surprisingly, latency to second CMAP peak showed an age-dependent delay, with increased latencies detected by 16 weeks of age in Hemi/Hom mice (Fig. S1H, S1J). Although the significance of this finding is not well understood, the increased latencies may signify a deficit in muscle hyperpolarization.

The profound muscle deficits observed in Hemi/Hom mice prompted us to examine the expression of transgenic PFN1^{C71G} in skeletal muscle to confirm the predominantly neuronal promoters used in the transgene constructs (Prp and human Thy1.2) did not leak expression into the muscle. We performed immunoblotting on skeletal muscle tissues from symptomatic 28-week-old Hemi/Hom mice and WT/Hemi controls. Even a long exposure of a Western blot probed with an antibody to recognize transgenic V5-PFN1^{C71G} did not reveal any exogenous expression of mutant PFN1 (Fig. S1K). Intriguingly, increased expression of endogenous mouse Pfn1 was observed in

(See figure on next page.)

Fig. 2 Phosphorylation of TDP-43 in the spinal cord and motor neuron degeneration precedes muscle dysfunction and motor deficits in Hemi/Hom PFN1^{C71G} transgenic mice. **A** Locomotor activity in an open field arena is reduced in Hemi/Hom (n = 22) mice relative to WT/Hemi (n = 23) controls (Mixed-effects analysis with Sidak's multiple comparisons). **B** Hemi/Hom (n = 22) mice show a progressive decline in rearing behavior in an open field arena (Mixed-effects analysis with Sidak's multiple comparisons). **C** Grip strength (forelimbs) and **D** rotarod performance decrease with age in Hemi/Hom mice (n = 22) compared to WT/Hemi (n = 23) animals (Mixed-effects analysis with Sidak's multiple comparisons). **E** Progressive hindlimb clasping in Hemi/Hom mice (n = 22). Mice were scored 0 to 5 according to the following parameters: 0 = limbs splayed outward; 1 = one limb retracted toward abdomen; 2 = two limbs retracted toward abdomen; 3 = three limbs retracted toward abdomen; 4 = four limbs retracted toward abdomen; 5 = all limbs retracted toward abdomen. **F** Gastrocnemius muscle weight decreases over time in Hemi/Hom mice (n = 8–10 per timepoint; One-way ANOVA with Dunnett's multiple comparisons) and H&E of muscle fiber changes in the gastrocnemius muscle. Progressive decline in **G** gastrocnemius muscle force (Kruskal–Wallis test with Dunn's multiple comparisons) and **H** CMAP amplitudes in Hemi/Hom mice (n = 8–10 per timepoint; Mixed-effects analysis with Dunnett's multiple comparisons). **I** Plasma neurofilament-light chain (Nf-L) levels in Hemi/Hom mice (n = 22) increase with age. **J** NMJ innervation declines before **K** terminal area reduction in tibialis anterior muscle of Hemi/Hom mice (n = 8–10 per timepoint). **L** NMJ innervation in the gastrocnemius muscle but not **M** terminal area declines in Hemi/Hom mice (n = 8–46 per timepoint). **N** Representative image of a capillary-based western of TDP-43 and V5-tagged PFN1^{C71G} protein in NP-40 soluble and NP-40 insoluble (urea soluble) protein fractions from Hemi/Hom mice of varying ages and 8-week-old strain-matched FVB/NJ WT controls. **O** Quantification of soluble and insoluble TDP-43 at different timepoints compared to WT controls (One-way ANOVA with Dunnett's multiple comparisons). **P** Representative western blot of phosphorylated TDP-43 protein in NP-40 insoluble (urea soluble) protein fraction from Hemi/Hom mice of varying ages and strain-matched 8-week-old FVB/NJ WT controls. **Q** Quantification of insoluble phosphorylated TDP-43 at different timepoints compared to WT controls (One-way ANOVA with Dunnett's multiple comparisons). **R** Immunohistochemistry of either TDP-43 (brown; i & ii) or phosphorylated TDP-43 (purple—serine 409/410; iii & iv) in mouse lumbar spinal cord from 32–35 week-old mice. WT controls showed expected TDP-43 and phosphorylated TDP-43 staining (i & iii). PFN1^{C71G} mice contain neurons with loss of nuclear TDP-43 and positive staining for TDP-43 in the cytoplasm (ii; black arrows). PFN1^{C71G} showed evidence of neuronal nuclear and cytoplasmic aggregates of phosphorylated pTDP-43 (iv; black arrows). Black and yellow outlines represent cell bodies and nuclei, respectively. **P < 0.05; **P < 0.01; ***P < 0.001; ****P < 0.0001.* Error bars represent s.e.m. and statistical tests were two-sided unless stated otherwise

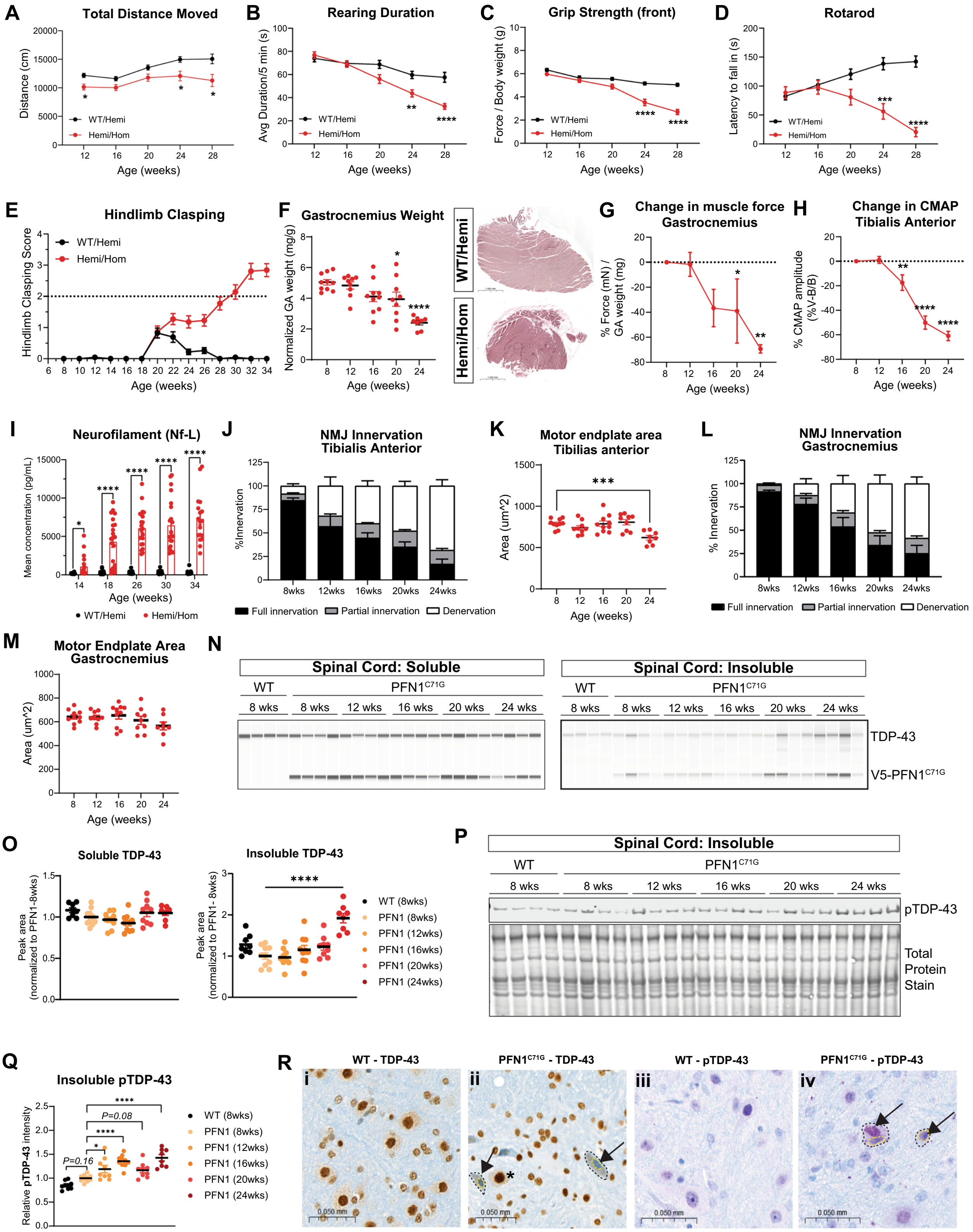

Fig. 2 (See legend on previous page.)

Hemi/Hom mice over WT/Hemi animals (Fig. S1K), suggesting Pfn1 may be upregulated in muscle by atrophy or injury.

Neurofilament light chain (Nf-L), an increasingly used biomarker of disease progression in ALS, is elevated in biofluids, such as blood, in people with ALS as a consequence of axonal degeneration. Consistent with progressive axonal degeneration, Nf-L levels in Hemi/Hom animals were significantly increased relative to WT/Hemi controls as early as 14 weeks of age and surged over time (Fig. 2I). The early onset of blood Nf-L elevation in Hemi/Hom animals, preceding CMAP amplitude reduction, prompted us to examine the timing of skeletal muscle denervation.

Tibialis anterior (TA) and gastrocnemius muscles were isolated from Hemi/Hom mice at different ages for NMJ analysis. NMJs in the TA, predominantly composed of fast-twitch muscle fibers, rapidly declined in Hemi/Hom with age, with only 56.9% of NMJs fully innervated at 12 weeks of age, representing a ~ 33% reduction from 8-week-old mice (Fig. 2J). In contrast, a slower decline in denervation was observed in the mixed fast- and slow-twitch gastrocnemius muscle. There, we observed a 14% reduction in fully innervated NMJs in 12-week-old Hemi/Hom mice from 8-week-old counterparts (Fig. 2L) that progressed to a ~ 75% reduction in fully innervated NMJs by 24-weeks of age (Fig. 2J, L), consistent with our previous finding (Fig. 1C, D). Similarly, a greater impact on NMJ terminal size was observed in the TA of Hemi/Hom mice; significant reduction in motor endplate area in TA NMJs was observed by 24 weeks of age (Fig. 2K), in contrast to the gastrocnemius, where no significant impact on motor endplate area was observed up to the same timepoint (Fig. 2M).

We next sought to confirm that CMAP and muscle force recordings correlate with NMJ innervation status to enable the use of these electrophysiological measurements to characterize the progression of muscle denervation in the same animal over time. We used the Pearson correlation coefficient analysis to determine a linear correlation between maximum CMAP amplitude in the TA with the percent of highly innervated TA NMJs, and performed the same analysis for the gastrocnemius, comparing muscle force in the gastrocnemius with percentage of highly innervated NMJs in the same muscle. A significant linear relationship between the variables were observed in both the TA ($r = 0.76$; $P < 0.0001$) and gastrocnemius ($r = 0.69$; $P < 0.0001$), indicating these in-life assays can be used as biomarkers for muscle denervation in PFN1^{C71G} transgenic mice (Fig. S1M, N).

Lastly, we determined the timing of insoluble pTDP-43 and TDP-43 induction in the spinal cord, having observed an increase in both protein species in phenotypic 28-week-old Hemi/Hom mice (Fig. 1J, K). To better understand their degree of TDP-43 pathology development, we chose to compare them to healthy, non-transgenic WT animals and not WT/Hemi mice, which have also been reported to develop a neurodegenerative phenotype, albeit with a delayed and slower progression than Hemi/Homs [22]. Henceforth, comparisons are made between Hemi/Hom and WT mice. Levels of insoluble TDP-43 in Hemi/Hom spinal cord tissues were largely maintained from 2 to 20 weeks of age, consistent with those from 8-week-old wild-type (WT) FVB/NJ controls, significantly increasing by 24 weeks of age while soluble TDP-43 levels remained unchanged in the spinal cord over the 24-week time period (Fig. 2N, O). In contrast, insoluble pTDP-43 protein levels increased in the same tissues over time, with significant elevation appearing in 12-week-old Hemi/Hom mice relative to 8-week-old Hemi/Hom mice (Fig. 2P, Q). A trend towards increased pTDP-43 was also observed in Hemi/Hom mice as early as 8 weeks of age relative to WT animals (Fig. 2P, Q), which sustained consistent pTDP-43 levels at all timepoints tested (Fig. S2). To corroborate these biochemical findings, we examined spinal cord tissues from PFN1^{C71G} mice for TDP-43 pathology and qualitatively observed that a minority of motor neurons displayed mislocalized TDP-43 as well as nuclear and cytoplasmic pTDP-43 inclusions (Fig. 2R). Immunohistochemistry was only done near end-stage (32–35 weeks of age), and therefore, we can not exclude the possibility that other motor neurons that have already degenerated may have also developed TDP-43 pathology. Importantly, spinal tissues obtained from WT controls exhibited no such visual evidence of TDP-43 pathology (Fig. 2R).

Furthermore, pTDP-43 in the spinal cord showed a significant negative correlation with NMJ innervation status in the TA muscle ($r = -0.501$; $P = 0.0004$; Fig. S1O) and less significantly with the GA muscle ($r = -0.359$; $P = 0.014$; Fig. S1P), suggesting fast-twitch muscle fibers are more vulnerable to TDP-43 pathology.

Given the increased incidence of ALS in men and numerous reports of sex differences in disease prognosis, we analyzed our PFN1^{C71G} data for sex-specific effects. We found male Hemi/Hom mice developed increased serum neurofilament levels (Fig. S3A) and an accelerated body weight decline (Fig. S3B) than females. Despite these signs of augmented disease progression, motor decline—as measured by rearing behavior (Fig. S3C), grip strength (Fig. S3D), rotarod performance (Fig. S3E), and hindlimb clasping (Fig. S3F) — and muscle function—assayed by both CMAP (Fig. S3G) and muscle force recordings (Fig. S3H)—progressed similarly between the sexes. Intriguingly, these data are consistent with a recent meta-analysis reporting a prevalence of weight loss in men with ALS without increased decline in functional ALSFRS-R scores, highlighting the potential translatability of our findings [23].

Taken together, our findings show that aberrant TDP-43 phosphorylation in the spinal cord is an early event in the course of neurodegeneration in triple transgenic PFN1^{C71G} mice, preceding the accumulation of insoluble non-phosphorylated TDP-43 protein, and occurring concomitantly with axonal degeneration, before the presentation of muscle dysfunction and, ultimately, motor impairment.

Reduction of Atxn2 by AAV-amiR-Atxn2 reduces insoluble pTDP-43 and TDP-43 in PFN1^{C71G} mice

Downregulation of Atxn2, a stress granule-associated protein, has been reported to mitigate neurotoxic TDP-43 aggregation and increase survival and motor function in the transgenic hTDP-43 (TAR4/4) mouse line [10, 13]. The functional effect of Atxn2 reduction in a non-TDP-43 overexpressing ALS mouse model, however, is unclear. Given the accumulation of insoluble TDP-43 in Hemi/Hom PFN1^{C71G} mice (hereafter referred to as PFN1^{C71G}), we tested whether chronic reduction of murine Atxn2 by viral delivery of an artificial *Atxn2*-targeting miRNA (AAV-amiR-Atxn2) could ameliorate TDP-43 pathology and improve disease progression.

A single bolus dose of either vehicle (DPBS + 0.001% Pluronic F-68) or AAV-amiR-Atxn2 (8E11vg total) was delivered intrathecally to PFN1^{C71G} mice at 6 to 9 weeks of age, when we previously observed the development of insoluble pTDP-43 accumulation in the spinal cord (Fig. 2Q). Age-, sex-, and strain-matched WT mice (FVB/NJ) were treated with vehicle as controls and mice were aged for 24 weeks after, with the study terminating before reaching euthanasia endpoints. A 54.8% reduction was observed in PFN1^{C71G} mice treated with AAV-amiR-Atxn2 relative to vehicle-treated WT controls (Fig. 3A) and showed selective expression of the amiR guide strand (Fig. 3B). To confirm knockdown at the protein level, cortical Atxn2 protein was assessed by immunoblotting with two distinct antibodies. Semi-quantification of the single co-localized band identified by both Atxn2-recognizing antibodies revealed a significant 35% and 22% reduction relative to vehicle-treated WT and PFN1^{C71G} mice, respectively (Fig. 3C).

Interestingly, a significant 12% reduction in *Atxn2* was detected in vehicle-treated PFN1^{C71G} spinal cord tissues (Fig. 3D), without accompanying expression of the amiR (Fig. 3E), suggesting neurodegeneration alone may reduce *Atxn2* expression. AAV-amiR-Atxn2 treatment in PFN1^{C71G} mice, however, decreased *Atxn2* mRNA even further, by 67.3%, compared to vehicle-treated WT controls (Fig. 3D) with concomitant expression of the amiR guide strand (Fig. 3E) and an average 40% decrement at the protein level (Fig. 3F).

Having confirmed sustained Atxn2 knockdown at both the mRNA and protein levels, we next assessed the effect of AAV-amiR-Atxn2 treatment on TDP-43 pathology by Western blotting for insoluble phosphorylated (S409/410) and non-phosphorylated TDP-43 in spinal cord tissue samples. Surprisingly, in addition to the primary pTDP-43 band observed in both WT and PFN1^{C71G} mice, a second, higher molecular weight pTDP-43 protein band was detected in samples generated from 34 to 36-week-old PFN1^{C71G} mice (Fig. 3G) that was absent in younger mice (Figs. 1J, 2Q). Although its exact identity is unclear, this larger protein likely represents hyperphosphorylated TDP-43 harboring additional post-translational modifications (i.e., ubiquitination, acetylation, phosphorylation at other protein residues), molecular features of advanced ALS-associated TDP-43 aggregates that likely develop with age in PFN1^{C71G} animals. Semi-quantification of both bands revealed a significant elevation in phosphorylated TDP-43 in vehicle-treated PFN1^{C71G} mice while pTDP-43 levels in those treated with AAV-amiR-Atxn2 were not significantly altered from WT controls (Fig. 3H). Increased insoluble accumulation of non-phosphorylated TDP-43 protein was also detected in vehicle-treated PFN1^{C71G} mice relative to WT mice, and Atxn2 reduction by amiR significantly restored insoluble TDP-43 back to WT levels (Fig. 3I). We next assessed whether AAV-amiR-Atxn2 altered levels of insoluble V5-tagged PFN1 protein levels or if its effect was specific to TDP-43. We found levels of mutant V5-tagged PFN1 insoluble protein were indistinguishable between vehicle-treated and AAV-amiR-Atxn2-treated mouse spinal cord tissues (Fig. 3J), indicating that the observed rescue of TDP-43 pathology by reduction of Atxn2 is not an effect of altered PFN1^{C71G} pathology. Together, these results demonstrate that Atxn2 expression is suppressed in the CNS of mice for as long as 28 weeks after a single treatment of a virally delivered amiR and prevents the development of TDP-43 proteinopathy.

Partial rescue of motor and muscle deficits in PFN1^{C71G} mice by AAV-amiR-Atxn2

We next determined the long-term effect of chronic Atxn2 reduction on neurodegeneration, muscle function, and motor decline in PFN1^{C71G} transgenic animals. AAVs have been reported to induce damage of dorsal root ganglion (DRG) neurons in several preclinical species, which can be detected by neurofilament release into the blood [24]. Consistent with these findings, increased blood

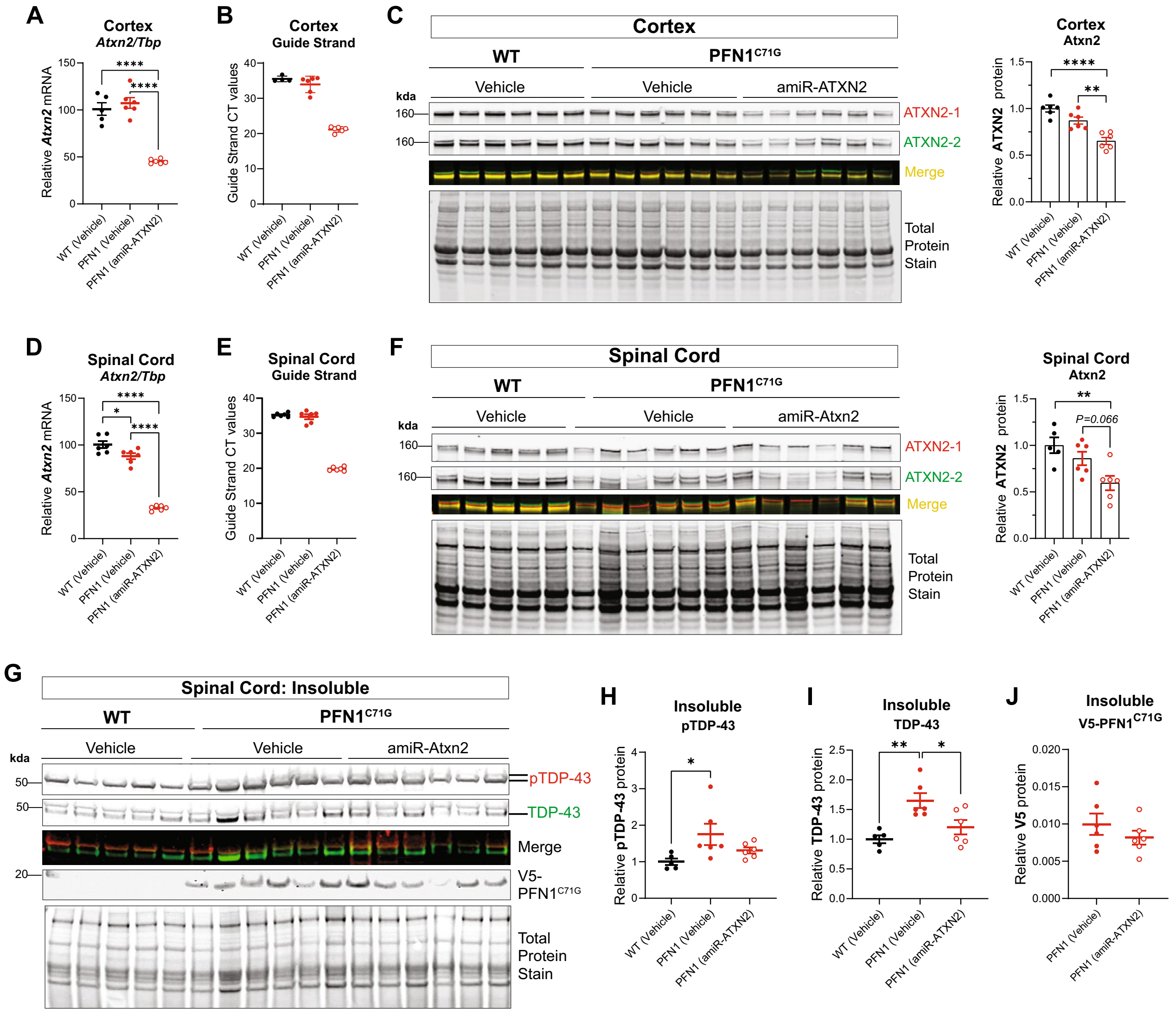

Fig. 3 Reduction of Atxn2 in PFN1^{C71G} animals by AAV-amiR-Atxn2 treatment reduces TDP-43 pathology in the spinal cord. **A** *Tbp*-normalized *Atxn2* mRNA levels in neocortical tissues isolated from 34 to 36-week-old vehicle- and amiR-Atxn2-treated PFN1^{C71G} mice relative to vehicle-treated WT mice (One-way ANOVA with Tukey's multiple comparisons). **B** RT-qPCR cycle threshold (CT) values of the amiR-Atxn2 guide strand obtained in the cortex of vehicle-treated WT mice and vehicle- and amiR-Atxn2-treated PFN1^{C71G} mice. **C** Representative western blot image of cortical Atxn2 protein levels detected by two different ATXN2 antibodies recognizing mouse Atxn2. Semi-quantification of the single co-localized band (yellow) is shown on the right (One-way ANOVA with Tukey's multiple comparisons). **D** *Tbp*-normalized *Atxn2* mRNA levels in spinal cord tissues isolated from 34 to 36-week-old vehicle- and amiR-Atxn2-treated PFN1^{C71G} mice relative to vehicle-treated WT mice (One-way ANOVA with Tukey's multiple comparisons). **E** RT-qPCR cycle threshold (CT) values of the amiR-Atxn2 guide strand obtained in the spinal cord of vehicle-treated WT mice and vehicle- and amiR-Atxn2-treated PFN1^{C71G} mice. **F** Representative western blot image of spinal cord Atxn2 protein levels detected by two different ATXN2 antibodies recognizing mouse Atxn2. Semi-quantification of the single co-localized band (yellow) is shown on the right (One-way ANOVA with Tukey's multiple comparisons). **G** Representative western blot image showing insoluble pTDP-43 at S409/410 (ticks demarcate two separate pTDP-43-positive bands in PFN1^{C71G} samples), TDP-43, and V5-tagged PFN1^{C71G} protein in age-matched WT and PFN1^{C71G} spinal cord lysates. **H** Semi-quantification of pTDP-43, **I** non-phosphorylated TDP-43, and **J** PFN1^{C71G} protein levels from western blot in (G) shows rescue of insoluble accumulation of pTDP-43 and TDP-43 but not PFN1^{C71G} in AAV-amiR-ATXN2-treated animals relative to controls. For all graphs, each point denotes an individual subject (WT-vehicle, n = 5–6; PFN1^{C71G}-vehicle, n = 6; PFN1^{C71G}-AAV-amiR-Atxn2, n = 5–6). Error bars represent s.e.m. and statistical tests were two-sided unless stated otherwise. *$*P < 0.05$; $**P < 0.01$; $***P < 0.001$; $****P < 0.0001$*

Nf-L levels were detected in AAV-amiR-Atxn2-treated PFN1^{C71G} mice immediately after dosing (Fig. 4A). This AAV-associated elevation in Nf-L waned over time as Nf-L began to rise in vehicle-treated PFN1^{C71G} mice. By 14 to 17 weeks of age, 8 weeks after dosing, both vehicle-treated and AAV-amiR-Atxn2-treated PFN1^{C71G} mice had significantly increased blood Nf-L amounts over age-matched WT animals. From there, Nf-L in vehicle-treated PFN1^{C71G} mice surged over time, peaking at 16 weeks post-injection. In contrast, amiR-Atxn2-treated mice displayed a slower rise in Nf-L, significantly diverging from vehicle-treated PFN1^{C71G} controls beginning at 12-weeks post-injection and for 12 weeks after. By 24 weeks post-injection, Nf-L in PFN1^{C71G} mice had only augmented to a level that was comparable to vehicle-treated PFN1^{C71G} mice 12 weeks prior, substantially lower than the maximal levels observed in vehicle-treated animals 16 weeks after dosing. We also observed a decline in mean levels of Nf-L in vehicle-treated PFN1^{C71G} mice from 16-weeks to 24-weeks post-injection, likely indicating a maximal amount of active neurodegeneration has already occurred in these animals as they approach end-stage, a phenomenon also seen in ALS [25]. In contrast, mean levels of neurofilament were still found to be rising in AAV-amiR-Atxn2 treated animals, indicating Atxn2 reduction delays neurodegeneration (Fig. 4A).

We next determined the effect of this observed delay in neurodegeneration on motor phenotypes in PFN1^{C71G} mice over time, comparing AAV-amiR-Atxn2-treated animals to vehicle-treated controls. For each animal, change from baseline was charted to normalize for variations in disease stage produced by the 3-week age gap within each group. AmiR-Atxn2-induced delay in Nf-L levels was associated with improved body weight gain and motor function in PFN1^{C71G} mice. While AAV-treated PFN1^{C71G} mice initially gained less body weight than PFN1^{C71G} controls, body weight gain continued to increase with age and was maintained for the duration of the study (Fig. 4B). This contrasted with vehicle treated PFN1^{C71G} mice, which only gained body weight 4 weeks after injection, with decline occurring 8 weeks later (Fig. 4B). Grip strength of forelimbs also declined more rapidly in vehicle-treated PFN1^{C71G} mice compared to those treated with AAV-amiR-Atxn2 (Fig. 4C). Hindlimbs were also similarly affected, with vehicle-treated PFN1^{C71G} mice displaying hindlimb clasping scores that were significantly elevated above those treated with AAV-amiR-Atxn2 (Fig. 4D). Open field behavior was altered in PFN1^{C71G} animals as previously observed, but those treated with AAV-amiR-Atxn2 exhibited improvements in locomotion (Fig. 4E) and vertical rearing behavior (Fig. 4F) compared to vehicle-treated counterparts. Furthermore, partial rescue of motor coordination was detected in PFN1^{C71G} mice with Atxn2 knockdown as measured by their significantly increased latencies to fall off an accelerating rotarod relative to vehicle-treated controls (Fig. 4G).

To correlate these amiR-Atxn2-induced improvements in motor behavior with muscle function, we performed histological and electrophysiological measurements in WT and PFN1^{C71G} muscles. GA isolated from 34 to 36-week-old vehicle-treated PFN1^{C71G} mice displayed marked disorganization of muscle fibers (Fig. 4I), and a reduction in lesser fiber diameter (Fig. 4J K), as previously observed in symptomatic 28-week-old mice (Fig.1F, G, H). Notably, average muscle fiber size (Fig. 4J) and size distribution (Fig. 4K) significantly improved with AAV-amiR-Atxn2 treatment, with associated increases in muscle force-frequency relationships (Fig. S4B). Maximum muscle specific force in the gastrocnemius was also improved by AAV-amiR-Atxn2 (Fig. 4H). Despite these improvements, CMAP electromyogram recordings from TA muscles of WT and PFN1^{C71G} mice, showed comparable decline in amplitudes between vehicle-treated and AAV-amiR-Atxn2-treated PFN1^{C71G} mice (Fig. S4A).

(See figure on next page.)

Fig. 4 AAV-amiR-Atxn2 treatment reduces blood neurofilament levels and improves muscle and motor function in PFN1^{C71G} transgenic mice. **A** Age-dependent rise in plasma Nf-L levels in PFN1^{C71G} mice is attenuated by AAV-amiR-Atxn2 treatment (WT-vehicle, n = 20; PFN1^{C71G}-vehicle, n = 20; PFN1^{C71G}-AAV-amiR-Atxn2, n = 21; Mixed-effects analysis with Tukey's multiple comparisons). **B** Body weight loss in PFN1^{C71G} mice is rescued by AAV-amiR-Atxn2 treatment. **C** Grip strength declines more gradually in PFN1^{C71G} mice treated with AAV-amiR-Atxn2. **D** Hindlimb clasping is partially rescued by AAV-amiR-Atxn2 in PFN1^{C71G} mice. **E** Progressive decline in locomotor activity in an open field arena is rescued by AAV-amiR-Atxn2 treatment in PFN1^{C71G} mice. **F** AAV-amiR-Atxn2 in PFN1^{C71G} mice produces a more gradual decline in vertical rearing behavior in an open field arena. **G** Rotarod performance in PFN1^{C71G} mice is significantly rescued by AAV-driven expression of an Atxn2-targeting amiR. For all motor behavior graphs, WT (vehicle), n = 17; PFN1^{C71G} (vehicle), n = 15; PFN1^{C71G} (AAV-amiR-Atxn2), n = 18 (One-way ANOVA with Tukey's multiple comparisons test). **H** Decline in gastrocnemius muscle force is significantly improved in PFN1^{C71G} mice given AAV-amiR-Atxn2. WT (vehicle), n = 15; PFN1^{C71G} (vehicle), n = 15; PFN1^{C71G} (AAV-amiR-Atxn2), n = 15 (Mixed-effects analysis with Tukey's multiple comparisons test). **I** Representative histological images from gastrocnemius muscles isolated from vehicle-treated WT and PFN1^{C71G} mice, and AAV-amiR-Atxn2-treated PFN1^{C71G} mice. **J** Muscle fiber lesser diameter is significantly increased in AAV-amiR-Atxn2-treated PFN1^{C71G} mice relative to vehicle-treated PFN1^{C71G} mice (One-way ANOVA with Tukey's multiple comparisons). **K** Histogram charting frequency distribution of muscle fiber lesser diameters in vehicle-treated WT (n = 5) and PFN1^{C71G} mice (n = 6), and AAV-amiR-Atxn2-treated PFN1.^{C71G} mice (n = 6). Error bars represent s.e.m. and statistical tests were two-sided unless stated otherwise. **P < 0.05; **P < 0.01; ***P < 0.001; ****P < 0.0001*

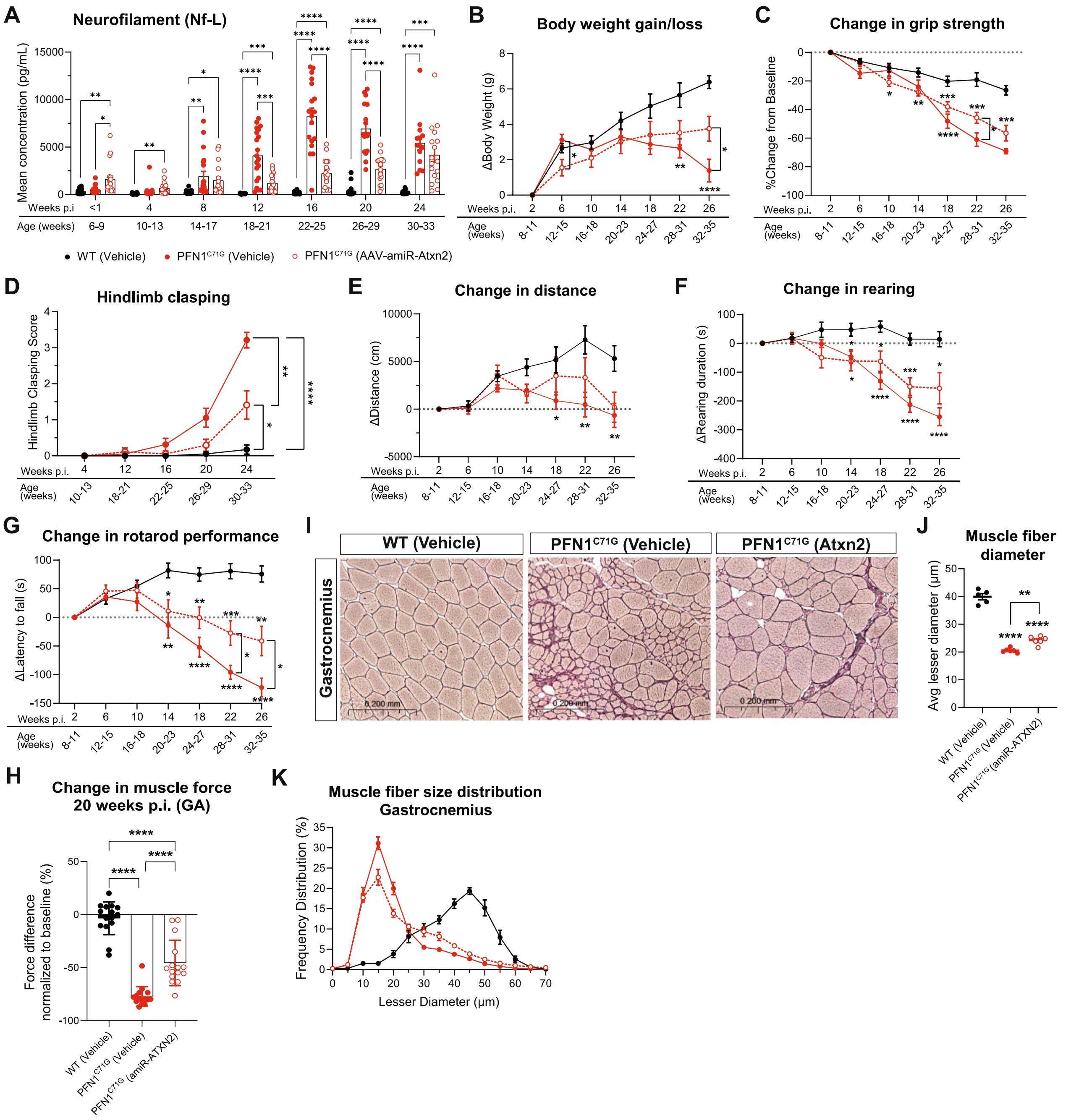

Fig. 4 (See legend on previous page.)

Reduction of immune-based genes in spinal cord and muscle tissues of PFN1^{C71G} mice following AAV-amiR-Atxn2 treatment

After observing significant benefit in the PFN1^{C71G} mice following AAV-amiR-Atxn2 treatment, we next determined the underlying molecular pathways dysregulated in the PFN1^{C71G} mice and whether AAV-amiR-Atxn2 treatment reversed these changes. Total RNA-sequencing was performed on spinal cord, cortex and TA skeletal muscle tissues collected at the study's end to determine differences in gene expression between wild-type mice and PFN1^{C71G} mice either treated with vehicle or AAV-amiR-Atxn2.

Among the three tissues examined, spinal cord and muscle tissue were primarily impacted in PFN1^{C71G} mice, with little change in the cortex relative to wild-type mice

(Fig. S5A-C), consistent with histopathological findings (Fig. S1B, C). In the spinal cord, PFN1^{C71G} vehicle treated mice had 2519 differentially expressed genes (1803 up and 716 down), whereas PFN1^{C71G} mice treated with AAV-amiR-Atxn2 showed a ~ 38% reduction in the number of differentially expressed genes (1565 total; 1209 up and 356 down) when compared to wild-type animals (Fig. 5A, B). Remarkably, there was a significant negative correlation between gene expression changes in the PFN1^{C71G} AAV-amiR-Atxn2 treated versus untreated mice and the changes in PFN1^{C71G} vehicle-treated versus wild type animals, suggesting the AAV-amiR-Atxn2 treatment reversed some of the dysregulation caused by the introduction of the PFN1^{C71G} transgene (Fig. 5C). We noted the most restored gene was *Gpnmb*. This was an intriguing finding as *GPNMB* mRNA has been reported to be highly elevated in ALS spinal cord and its expression negatively correlated with disease duration [26, 27], suggesting the reduction of *Gpnmb* observed in our model after AAV-amiR-Atxn2 treatment may be partly contributing to the behavioral benefits observed in this study. Furthermore, we observed significant restoration of *ChAT* expression in PFN1^{C71G} mice after AAV-amiR-Atxn2 treatment, indicating motor neuron recovery in the spinal cord (Fig. S5D).

A gene set enrichment analysis using gene ontology (GO) biological terms showed that the genes dysregulated in PFN1^{C71G} mouse spinal cord were overwhelmingly overrepresented in innate/adaptive immune responses and various inflammatory pathways (Fig. 5D). To determine if Atxn2 reduction could alter the expression of these immune-related genes, we examined the transcripts related to the term "immune response", one of the most upregulated GO terms in vehicle-treated PFN1^{C71G} mice, and found that AAV-amiR-Atxn2 treatment did indeed attenuate their expression, bringing them closer to wild-type levels (Fig. 5E). Examination of hallmark genes sets revealed several immune-based pathways that may contribute to the disease phenotype in PFN1^{C71G} mice, including Tnfα signaling via NFkB, and the interferon gamma and complement pathways (Fig. 5F). Interestingly, heavy dysregulation of cholesterol homeostasis was also observed in the PFN1^{C71G} model, which was partially rescued by AAV-amiR-Atxn2 treatment (Fig. 5G). Several cholesterol regulatory genes (*Ldlr, Dhcr24, Msmo1, Idi1* and *Hmgcs1*) were significantly downregulated in PFN1^{C71G} mice, which has similarly been observed in the Atxn2-CAG100 ALS mouse model [28], and partially rescued by Atxn2 knockdown. This finding indicates that PFN1^{C71G} mice may be appropriate to assess the consequences related to ALS-associated cholesterol dysregulation in the spinal cord and further highlights the role of Atxn2 in cholesterol homeostasis. Significantly altered splicing of previously reported mouse TDP-43 RNA targets, however, were not observed in our bulk RNA-seq analysis (data not shown), likely due to the limitation of bulk RNA-seq analyses in detecting splicing changes produced by a small minority of cells exhibiting TDP-43 pathology, as also observed in ALS.

Despite the PFN1^{C71G} transgene being exclusively expressed in neurons, PFN1^{C71G} transgenic mice

(See figure on next page.)

Fig. 5 AAV-amiR-Atxn2 treatment attenuates immune-based responses in both spinal cord and muscle tissues of PFN1^{C71G} mice. RNA-sequencing analysis of either spinal cord (A-G) or skeletal muscle tissue (H-N). **A**–**B** Volcano plots showing changes in gene expression in spinal cord of PFN1^{C71G} mice treated with either vehicle (A) or AAV-amiR-Atxn2 (B) compared to wild-type animals treated with vehicle (n = 6). Red and dark blue dots represent upregulated and downregulated genes, respectively, with > twofold change and padj < 0.05. Orange and light blue dots represent significantly upregulated and downregulated genes, respectively, with < twofold change and padj < 0.05. **C** Correlation of gene expression changes when PFN1^{C71G} vehicle treated animals are compared to wild-type vehicle treated or PFN1^{C71G} AAV-amiR-Atxn2 treated mice. Pearson correlation coefficient (r) was used to determine the linear correlation between the two conditions. Purple dots represent genes that were significantly changed (padj < 0.05) in either condition. Grey dots represent genes that had a padj > 0.05 in both conditions. **D** Bubble plot of the top 20 gene ontology (GO) terms based on dysregulated genes that have a ≥ twofold change and padj < 0.05 in the spinal cord of PFN1^{C71G} mice. **E** Heatmap of gene expression changes in GO immune response across groups. **F** Enriched hallmark gene sets based on dysregulated genes that have a ≥ twofold change and padj < 0.05 in the spinal cord of PFN1^{C71G} mice. **G** Heatmap of gene expression changes in the cholesterol homeostasis hallmark gene set across groups. **H**–**I** Volcano plots showing changes in genes expression in the skeletal muscle of PFN1^{C71G} mice when treated with either vehicle (H) or AAV-amiR-Atxn2 (I) compared to wild-type animals treated with vehicle (n = 6). Red and dark blue dots represent upregulated and downregulated genes, respectively, with > twofold change and padj < 0.05. Orange and light blue dots represent significantly upregulated and downregulated genes, respectively, with < twofold change and padj < 0.05. **J** Correlation of gene expression changes when PFN1^{C71G} vehicle treated animals are compared to wild-type vehicle treated or PFN1^{C71G} AAV-amiR-Atxn2 treated mice. Pearson correlation coefficient (r) was used to determine the linear correlation between the two conditions. Purple dots represent genes that were significantly changed (padj < 0.05) in either condition. Grey dots represent genes that had a padj > 0.05 in both conditions. **K** Bubble plot of the top 20 gene ontology (GO) terms based on dysregulated genes that have a ≥ twofold change and padj < 0.05 in the skeletal muscle of PFN1^{C71G} mice. **L** Heatmap of gene expression changes in GO immune response across groups. **M** Enriched hallmark gene sets based on dysregulated genes that have a ≥ twofold change and padj < 0.05 in the skeletal muscle of PFN1^{C71G} mice. **N** Heatmap of gene expression changes in the myogenesis hallmark gene set across groups

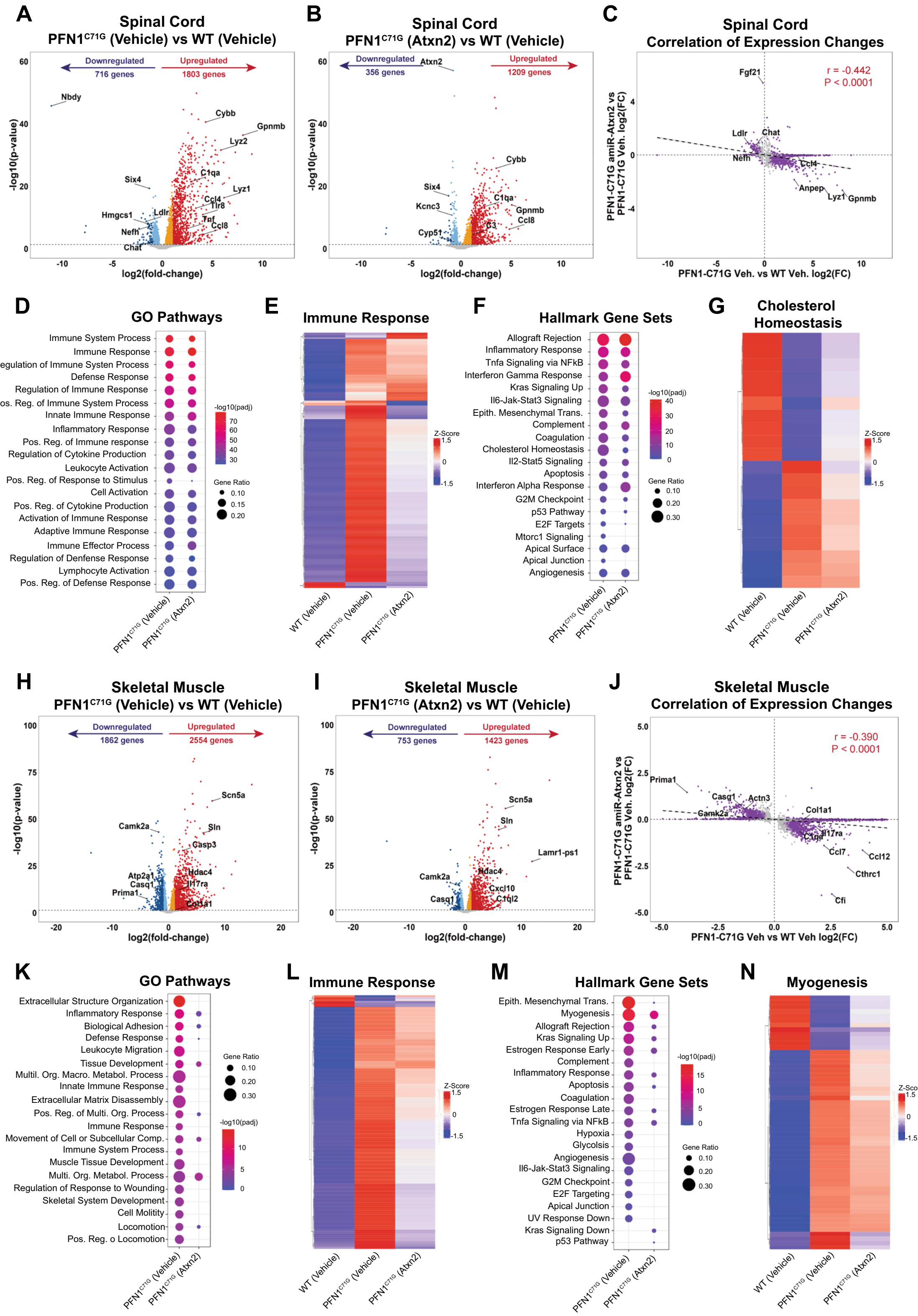

Fig. 5 (See legend on previous page.)

showed a surprisingly large amount of gene expression dysregulation within the TA muscle. Compared to vehicle-treated WT mice, TA tissues from vehicle-treated PFN1^{C71G} mice had 4416 differentially expressed genes (2554 up and 1862 down), while the number of differentially expressed genes was reduced by more than half in PFN1^{C71G} mice treated with AAV-amiR-Atxn2 (2176 total; 1423 up and 753 down; Fig. 5H,I). Furthermore, a significant negative correlation in gene expression was observed from vehicle-treated PFN1^{C71G} mice compared to either WT controls or PFN1^{C71G} AAV-amiR-Atxn2-treated animals, indicating that AAV-amiR-Atxn2 treatment reversed gene expression changes in PFN1^{C71G} TA muscle to that of WT (Fig. 5J). As was observed in the spinal cord, PFN1^{C71G} mice showed an enrichment of many inflammatory and immune response related GO gene sets, suggestive of a developed immune-mediated myositis. Notably, differentially expressed genes in AAV-amiR-Atxn2 treated PFN1^{C71G} mice did not show enrichment in immune-based GO terms when compared to WT animals, indicating a drastic reduction in the upregulation of immune processes in the skeletal muscle following AAV-amiR-Atxn2 treatment (Fig. 5K). Further examination of the gene expression changes within the GO-term "immune response" revealed a partial rescue of the expression changes in immune-based transcripts following AAV-amiR-Atxn2 treatment (Fig. 5L). Analysis of hallmark gene sets showed that many of the enriched pathways within the PFN1^{C71G} mouse skeletal muscle were either rescued or had their dysregulation reduced after AAV-amiR-Atxn2 treatment, including several immune pathways such as the complement pathway, Il6-Jak-Stat3 pathway, inflammatory response and Tnfα Signaling via NFkB (Fig. 5M). Furthermore, a partial rescue in myogenesis was observed in AAV-amiR-Atxn2-treated mice, evidence of muscle recovery at the molecular level consistent with the observed rescue in muscle atrophy and function (Fig. 5M, N). In line with finding increased levels of endogenous muscle mouse Pfn1 protein in symptomatic PFN1^{C71G} mice (Fig. S1K), mouse *Pfn1* transcripts were also significantly increased in vehicle-treated PFN1^{C71G} TA muscle by RNA-seq analysis ($P = 0.000734$) but not in AAV-amiR-Atxn2-treated mice ($P = 0.413$). We verified these benefits did not occur due to leakage of AAV-amiR-Atxn2 in the muscle, as *Atxn2* expression was comparable in TA muscle tissues across all groups (Fig. S4C). Taken together, these findings highlight robust dysregulation of gene expression in affected organs of PFN1^{C71G} mice and the development of immune-mediated transcriptional responses in both spinal cord and skeletal muscle that are partially reversed by pre-symptomatic reduction of Atxn2 in the CNS, with greater dysregulation and recovery observed in muscle.

PFN1^{C71G} mice show similar transcriptional dysregulation in the spinal cord as ALS

Having shown that PFN1^{C71G} mice develop several ALS-relevant spinal cord phenotypes including the formation of pTDP-43 aggregates, motor neuron degeneration, and motor deficits, we asked whether the molecular pathways dysregulated in the PFN1^{C71G} animals also occur in ALS to build further confidence in the translatability of this mouse model.

Post-mortem spinal cord RNA-seq datasets from Target ALS (GSE153960), comprised of C9orf72-ALS and SOD1-ALS cases, and the University of Miami (UMiami; manuscript under preparation), which contained sporadic ALS (sALS) cases, were used for differential gene expression analysis. For Target ALS, raw fastq files from spinal cord datasets were downloaded from the publicly available Target ALS Postmortem Tissue Core repository. For UMiami, frozen transverse sections of lumbar spinal cords from sALS and neurologically healthy control participants were purchased from University of Miami Brain Bank. We found evidence of transcriptional dysregulation in the cervical, thoracic, and lumbar spinal cord in ALS samples from the Target ALS dataset and in the lumbar spinal cord of sALS samples obtained from the UMiami dataset (Fig. S6A–D). We then compared these ALS-associated gene expression changes to those in PFN1^{C71G} mice and determined that the genes that were significantly dysregulated in ALS spinal cord tissues also showed large gene expression changes in PFN1^{C71G}

(See figure on next page.)

Fig. 6 WGCNA identifies preserved expression changes in the spinal cord of PFN1^{C71G} transgenic mice and individuals with ALS. **A** Heatmaps showing gene expression changes in PFN1^{C71G} spinal cord of transcripts identified to be dysregulated in different ALS spinal cord regions (cervical, thoracic, and lumbar). **B** Module eigen genes from PFN1^{C71G} mice in vehicle-treated WT and PFN1^{C71G} mice and AAV-amiR-Atxn2-treated PFN1^{C71G} mice. *Signifies that the adjusted p value of t-test is < 0.05. **C** Left: preservation score of PFN1^{C71G} mice modules in sporadic ALS from University of Miami dataset. Right: lightcoral and mediumpurple2 module eigen genes in sporadic ALS. **D** Left: preservation score of PFN1^{C71G} mice modules in C9orf72 Target ALS dataset. Right: lightcoral and mediumpurple2 module eigen genes in C9orf72 Target ALS. **E** Left: preservation score of PFN1^{C71G} mice modules in SOD1 Target ALS dataset. Right: lightcoral and mediumpurple2 module eigen genes in SOD1 Target ALS. **F** Overlapped lightcoral module hub genes and DEGs in PFN1^{C71G} mice vs WT mice and human ALS vs control dataset. **G** Overlapped mediumpurple2 module hub genes and DEGs in PFN1^{C71G} mice vs WT mice and human ALS vs control dataset

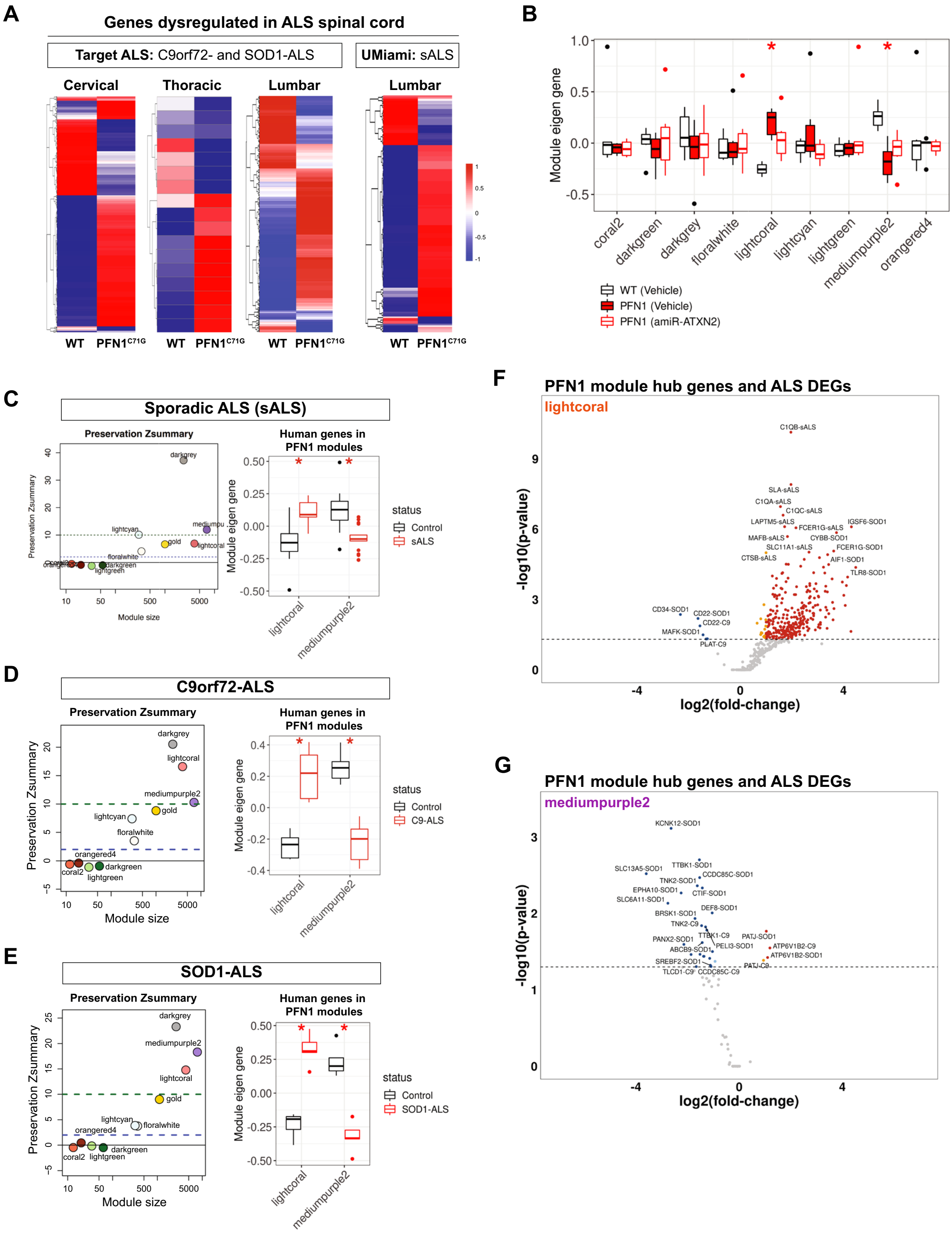

Fig. 6 (See legend on previous page.)

mouse spinal cord when compared to WT animals (Fig. 6A), indicative of shared patterns of transcriptional dysregulation between PFN1^{C71G} mouse and human ALS spinal cord.

To gain insight into the biological pathways affected in both mouse and human datasets, we first performed a weighted gene correlation network analysis (WGCNA) utilizing RNA-sequencing data from PFN1^{C71G} spinal cord samples. WGNCA on PFN1^{C71G} mouse spinal cord revealed 9 gene co-expression modules. Two of these modules, lightcoral and mediumpurple2, were significantly increased and decreased, respectively, in PFN1^{C71G} mice compared to wild-type mice and, notably, partially rescued by AAV-amiR-Atxn2 treatment (Fig. 6B). Further analysis of the lightcoral gene set showed an enrichment for pathways related to immune-based responses, including a neuroinflammation signaling pathway, STAT3 signaling, toll-like receptors cascades, and several interleukin signaling pathways. The mediumpurple2 gene set, in contrast, was enriched for pathways more associated with neuronal function, such as synaptogenesis and SNARE signaling pathways, as well as genes associated with autophagy which are known to be dysregulated in ALS (Fig. S6E).

To determine if these gene sets were translatable to ALS, we looked for module preservation by examining network homology between PFN1^{C71G} and ALS WGCNA datasets. This analysis revealed strong preservation of the darkgrey module across all ALS post-mortem datasets (Fig. 6C, D, E), which was unchanged in expression between WT, vehicle-, and AAV-amiR-Atxn2-treated PFN1^{C71G} mice (Fig. 6B). Further analysis of the darkgrey module revealed genes enriched in foundational regulatory pathways that control cell cycle and transcription, which likely underlie its strong preservation given the essential nature of these biological pathways. Remarkably, both of the PFN1^{C71G}-dysregulated lightcoral and mediumpurple2 gene sets were highly preserved across all ALS groups and, moreover, were similarly upregulated and downregulated, respectively, as observed in PFN1^{C71G} mice (Fig. 6C, D, E). The widespread preservation of the lightcoral and mediumpurple2 modules may indicate the disparate biological mechanisms underlying these distinct forms of ALS converge onto these module pathways, potentially leading to shared clinical features. Together, these data reveal a shared upregulation of neuroinflammation and downregulation of neuronal function in PFN1^{C71G} mice and ALS individuals.

Intramodular hub genes are central, highly connected genes within a given module that have been shown to represent biologically relevant disease traits, and as such, possess potential as therapeutic targets. Given that the lightcoral and mediumpurple2 modules are conserved between PFN1^{C71G} mice and ALS spinal cord samples, we next identified hub genes of interest by identifying those that showed differential expression in both ALS and PFN1^{C71G} spinal cord tissues. Intriguingly, we observed several of the upregulated hub genes in the lightcoral gene set corresponded to the complement pathway, including *C1QA*, *C1QB* and *C1QC* in sALS (Fig. 6F), suggesting the complement pathway is activated in both sALS and PFN1^{C71G} mice and may further drive transcriptional dysregulation in the spinal cord. Downregulated hub genes in the mediumpurple2 module, meanwhile, were mostly DEGs shared with SOD1- and C9orf72-ALS cases (Fig. 6G). Of note, the TDP-43 kinase, *Tau-tubulin kinase 1* (*TTBK1*), which has been implicated in ALS, was identified as dysregulated in both SOD1 and C9orf72-ALS [29, 30]. Collectively, these findings point to PFN1^{C71G} mice as a highly translatable model of ALS, both molecularly and functionally, and a potential resource to identify and validate new therapeutic targets for ALS.

Discussion

Previous work to model TDP-43 proteinopathy in rodents has primarily manipulated TDP-43 expression itself, either through exogenous expression to induce phosphorylated, cytoplasmic TDP-43 aggregates or through knockdown and genetic ablation to abolish TDP-43 function. However, elevated levels of nuclear TDP-43 have been found to induce aberrant exon skipping, a phenomenon that does not correlate with ALS, while loss of TDP-43 function alone models a single aspect of TDP-43 pathology [14, 31]. TDP-43 dysfunction has also been observed in the ATXN2-CAG100 mouse line; however, this model requires prolonged aging to develop TDP-43 pathology (~ 14-months), limiting its use in drug discovery and development efforts [27].

In this study, we performed a comprehensive characterization and phenotypic timeline (Fig. S7) of a previously published transgenic mouse model of ALS expressing the ALS-causing mutation, PFN1^{C71G}, which was reported to develop progressive motor neuron degeneration and muscle weakness within half a year of life, while transgenic mice expressing wild-type PFN1 were indistinguishable from non-transgenic controls. We found that neuronal overexpression of PFN1^{C71G} produces a Wallerian-like degeneration of motor axons that induces muscle denervation and atrophy before significant loss of lower motor neuron cell bodies in the spinal cord. Consistent with this finding, RNA-seq data from WT and PFN1^{C71G} mice show little alteration of gene expression in the cortex relative to the spinal cord and skeletal muscle, with the transcriptome in skeletal muscle showing the most profound dysregulation amongst all 3 organs. Notably, we observed TDP-43 pathology in the spinal cord of PFN1^{C71G} mice, with accumulation of detergent-insoluble phosphorylated TDP-43 occurring as early as 8–12 weeks of age, preceding the buildup of non-phosphorylated TDP-43. This timing contrasts with previous findings of insoluble TDP-43 increasing prior to the phosphorylation of the protein [32]. These studies, however, incorporated TDP-43 overexpression systems, which may promote aggregation kinetics that differ from those that occur physiologically. Importantly, this induction of detergent-insoluble phosphorylated TDP-43 inclusions in PFN1^{C71G} mice enables us to test the functional effect of attenuating TDP-43-associated toxicity through strategies such as the one undertaken in this study without the confounds of TDP-43 overexpression.

In support of PFN1's role in maintaining neuronal integrity, another transgenic mouse model of ALS overexpressing the ALS-associated PFN1 mutation (PFN1^{G118V}) was reported to develop ALS-like motor phenotypes [33]. Interestingly, the more severe PFN1^{G118V} model was found to develop upper motor neuron degeneration, in contrast to the PFN1^{C71G} mice where the cortex is spared. However, while PFN1^{G118V} mice show an increase in pTDP-43 expression by immunohistochemistry, these animals do not appear to develop mislocalization of TDP-43 from the nucleus or form cytoplasmic pTDP-43 and TDP-43 aggregates that are observed in the PFN1^{C71G} model. Thus, while both models replicate several features of the disease, the major advantage for the PFN1^{C71G} model is its ability to recapitulate TDP-43 proteinopathy, a critical pathological hallmark of ALS.

A key characteristic of ALS is the denervation of NMJs and resultant muscle atrophy, yet the molecular changes that transpire in skeletal muscle have been understudied in the ALS field relative to the brain and spinal cord. In PFN1^{C71G} mice, we observed NMJ denervation as early as 12 to 16 weeks within the TA and GA muscles, before the manifestation of motor phenotypes. Furthermore, NMJ denervation in the GA muscle is delayed compared to TA muscle, suggesting earlier degeneration of motor neurons associated with fast-twitch muscle fibers, as has been observed in people with ALS. Surprisingly, electrophysiological measurements of muscle function and activity (CMAP in the TA and force in the GA) was only rescued by AAV-amiR-Atxn2 in the GA and not the TA. Given the disparate results seen in the TA and GA muscles, we speculate that Atxn2 reduction needs to be either greater or induced earlier to have impact on the TA muscle due to its more rapid NMJ loss.

Notably, we found the TA muscle of PFN1^{C71G} mice had the greatest number of dysregulated transcripts of all tissues tested, exceeding the spinal cord, that was partially corrected by Atxn2 reduction in the central nervous system. In the TA muscle of PFN1^{C71G} mice, we observed an upregulation in immune-based responses that are associated with muscle denervation and atrophy, such as the Il6-Jak-Stat3 signaling pathway [34]. AAV-amiR-Atxn2 treatment reduced muscle atrophy in PFN1^{C71G} mice, which corresponded with a strong reduction in immune-based gene expression in muscle tissue. This was surprising, as the AAV therapy had no impact on the expression of Atxn2 in the muscle tissue. However, ALS is not classically defined by myositis, underscoring the need for further investigation into the biological underpinnings of the observed muscle inflammation in PFN1^{C71G} mice, the timing of its development during the disease course, and its relevance to ALS.

It is important to note that these results showing benefit of Atxn2 knockdown in PFN1^{C71G} animals contradict the recent negative results of the Phase I/II clinical trial ALSpire (clinicaltrials.gov number NCT04494256), in which an intrathecally-administered antisense oligonucleotide designed to degrade ATXN2 mRNA yielded no benefit in people living with ALS. However, the work presented in this manuscript administered treatment in the PFN1^{C71G} mouse model around the onset of TDP43 pathology development and before the manifestation of muscle weakness and motor deficits. In contrast, individuals with ALS are not treated until after symptom onset. Whether Atxn2 knockdown would be effective in ameliorating disease phenotypes after the onset of neurodegeneration, which would more closely model the circumstances for people with ALS, is still an outstanding question. Future work is needed to determine whether post-symptomatic reduction of Atxn2 can also slow disease progression in PFN1^{C71G} mice, or if its inhibition primarily prevents the development of TDP-43 pathology, rendering it an ineffective target once TDP-43 inclusions are formed. A potential difference in disease pathophysiology between mice and humans may also underlie the discrepancy in results.

The identification and development of highly translatable mouse models of ALS are required for the development of clinically meaningful therapies. Through extensive examination of the PFN1^{C71G} model, a non-TDP-43 overexpression ALS mouse model, we find high construct and face validity to ALS for several reasons. First, it is a progressive motor neurodegenerative model that develops ALS-like phenotypes and, importantly, develops hyperphosphorylated TDP-43 aggregates in the spinal cord as observed in ALS. Second, we find significant overlap in dysregulated molecular pathways between PFN1^{C71G} mice and human ALS. However, the RNA-seq analyses in this study and in those incorporating post-mortem ALS tissues only capture a snapshot of transcriptional dysregulation at/near endstage, which may not necessarily reflect the pathological process. Thus, future work is required to determine whether these shared molecular changes drive disease or are secondary to the pathological process, which can be assessed in the PFN1^{C71G} model.

Another major advantage of the PFN1^{C71G} model over other TDP-43 overexpression models is its more slowly progressing phenotype, providing the opportunity to intervene therapeutically at various points during disease progression and determine expected treatment outcomes when therapies are delivered at a later disease state. One caveat, however, is that PFN1^{C71G} overexpression, which we found unaffected by Atxn2 reduction, is the main disease driver in this model. This could suggest that pTDP-43 is a marker of neuronal injury or cellular stress but not necessarily the pathomechanism of neuronal death in this model. Therefore, mitigation of TDP-43 pathology alone, without attenuation of PFN1^{C71G} pathology, may only enable partial rescue of phenotypes, potentially creating a ceiling effect that warrants further investigation.

While several others have shown mutant PFN1 overexpression can lead to an increase in phosphorylated TDP-43 cytoplasmic aggregates in human and mouse in vitro systems [19, 20], similar to what we have shown here in vivo, there is still a lack of knowledge into how mutant PFN1 expression induces TDP-43 pathology. One potential hypothesis is that mutant PFN1 disrupts the proteasome pathway leading to ER stress that induces TDP-43 phosphorylation and aggregation [20]. However, this has not been directly tested and needs to be addressed to further understand what factors contribute to TDP-43 pathology in the presence of mutant PFN1 and where we may be able to therapeutically intervene.

Collectively, our study illustrates the molecular, transcriptional, and functional changes in the brain, spinal cord, and skeletal muscle tissues of the PFN1^{C71G} ALS mouse model, demonstrating the progression of disease in these animals and their relevance to ALS. A single intrathecal injection of AAV-amiR-Atxn2 was sufficient to reduce Atxn2 expression for ~ 28 weeks and mitigate TDP-43 pathology and ALS-relevant phenotype development in both the spinal cord and skeletal muscle tissues despite continued expression of transgenic PFN1^{C71G}. Importantly, while the spinal cord remains the source of disease pathogenesis in these mice, our study also highlights the profound effects of neurodegeneration on skeletal muscle, underscoring the need for a better understanding of its role in disease progression.

Methods

Animals

The C71G mutant PFN1 transgenic mice were generated by Zuoshang Xu's laboratory and have been described previously [22]. The PFN1^{C71G} triple transgenic mice (FVB/N-Tg(Prnp-PFN1*C71G)22Zxu Tg(Thy1-PFN1*C71G)67Zxu/J, stock # 028608), PFN1^{C71G} single transgenic mice (Tg(THY1-PFN1*C71G)67Zxu, stock # 028608), and age-matched wildtype FVB/NJ controls (stock # 001800) were purchased from Jackson Laboratory (Bar Harbor, Maine) and the study cohort was bred internally at Biogen. All animal experiments are compliant with the guidelines of Biogen Animal Care and Use Committee (IACUC) and followed by National Institute of Health Guide for the Care and Use of Laboratory Animals.

Viral preparation and administration

The targeting sequence for murine ATXN2 was originally purchased as a lentiviral cassette from Transomic (cat. ULTRA-3236441). The sense-loop-antisense sequence CCAGCCCATTCCAGTCTCGACA-TAGTGAAGCCACAGATGTA-TGTCGAGACTGGAATGGGCTGT was subsequently cloned into a ssAAV cassette with a CAGG promoter driving the targeting sequence embedded in a miRE cassette followed by an hGH polyA terminator. Initial AAV-PHP.eB-mATXN2-amiR-E-41 (AAV-amiR-ATXN2) material was produced, purified, and purchased from Packgene (Lot. 8889).

Mice were anesthetized with 2% isoflurane gas anesthesia and was maintained by a nose cone. Each animal was injected between the L4 and L5 spinal segments and a tail-flick indicated successful needle insertion. The proper amount of injection solution (10 μL) was injected by 29-gauge syringe.

Animal behavior

All behavioral testing was counterbalanced across experimental groups. Mice were acclimated to the testing room for a minimum of 30 min prior to undergoing motor behavior tests.

Hindlimb clasping

Mice were lifted by the base of their tail and suspended for approximately 10 s to assess limb clasping. Mice were scored 0 to 5 according to the following parameters: 0 = limbs splayed outward (away from abdomen); 1 = one limb retracted toward abdomen; 2 = two limbs retracted toward abdomen; 3 = three limbs retracted toward abdomen; 4 = four limbs retracted toward abdomen; 5 = all limbs retracted toward abdomen and body forming a ball.

Grip strength

Grip strength was assayed using the grip strength meter (TSE Systems), which measures mechanical force exerted on a small bar/grid. Mice were allowed to grip (forelimbs) a small metal bar connected to a force-measuring device. The animal was then gently pulled horizontally until it lost its grip. The process was repeated until at least 3 measurements were recorded on the TSE computer program. Mice were allowed to rest for a minimum of 5 min between tests.

Rotarod

For each trial, mice were placed in one of five lanes on the rotating rod (Ugo Basile) programmed to accelerate from 12 to 72 rpm (revolutions per minute) over 5 min. Each mouse received three trials with a minimum 10-min interval between each trial. When the mice fell onto the trip box, the latency to fall was recorded. If mice did not fall from the rotarod, they were removed at 5 min. The best performance out of the three trials was used for analysis.

Open field assay

Mice were individually placed in a cylindrical arena approximately 43 cm in diameter and allowed to free-roam. An overhead camera was used to track the animals through Noldus Ethovision 15 for 30 min of testing time.

CMAP

Animals were anesthetized with 1.5–2.5% isofluorane and a set of 5 electrodes (ground, recording, reference, stimulation, and return) were inserted into the appropriate locations in the body, with the ground electrode inserted subcutaneously in the upper back, the recording electrode 1 mm into the TA muscle, the reference electrode near the ankle, the stimulation electrode 10 mm lateral to the midline reference point in a near-vertical orientation, and the return electrode approximately 3-5 mm lateral to the midline reference point. The proper current level to generate a CMAP was determined. Once the maximum CMAP amplitude was achieved, the current was increased one more step to achieve a supramaximal stimulation level and the CMAP results were recorded.

Triggered dual-mode lever assay

First, a ‘twitch’ protocol was used to optimize stimulation and muscle length parameters to ensure the muscle is under ideal conditions to generate maximal force (0.1-0.2 ms, 1000 Hz). ‘Tetanic’ protocol was utilized to measure the maximum force generated by the muscle (100-150 Hz). A force-frequency correlation protocol was also performed, which involves stimulation of the muscle at frequencies from 10–150 Hz for 200-500 ms with 1 min rest time in between each stimulation following a ‘twitch’ and a ‘tetanus’ protocol.

Neurofilament-light (Nf-L) measurements

Blood Nf-L levels were measured from serum samples using the Simple Plex Human Nf-L Cartridge (ProteinSimple, SPCKB-PS-002448) according to the manufacturer’s guidelines. In brief, serum samples were thawed, brought to room temperature, and diluted 1 to 6 in Sample Diluent SD13 buffer (R&D Systems, 896,098). Samples were mixed and 50uL volumes were transferred to wells within the Simple Plex cartridge per manufacturer’s guidelines. The cartridge was run on the Ella Automated Immunoassay system (ProteinSimple, 600–100) using the Simple Plex Runner software.

Tissue processing

Mice were euthanized by CO2 asphyxiation as approved by the IACUC protocol. For RNA and protein analysis, neocortex, cervical/thoracic region of the spinal cord, and TA muscle tissues were dissected, snap frozen in liquid nitrogen, and then stored at -80 °C until processing. Frozen tissues were lyophilized into powder using the Geno/Grinder (Cole-Parmer Spex). For immunohistochemical analysis, the lumbar/sacral region of the spinal cord, brain and GA muscle were drop-fixed in 10% NBF and eventually paraffin embedded.

Immunohistology

Lumbar/sacral spinal cord, brain and muscle tissues were sectioned into 5um slices.

Immunohistochemistry staining

Immunohistochemistry was performed using the fully automated Ventana Discovery Ultra. Primary antibodies, either rabbit anti-ChAT (Abcam, 178,850), rabbit anti-TDP-43 (Proteintech, 10,782–2-AP), rabbit anti-pTDP-43 (Cosmo Bio, CAC-TIP-PTD-P07), or chicken anti-V5 (Novus Bio, NB600-379) were incubated for 1-h at RT. Slides were incubated at 36 °C with anti-Rabbit NP (Roche, 07425317001) and Anti-NP AP (Roche, 07425325001) probes followed by Discovery Red kit (Roche, 07425333001) were used to visualize ChAT positive areas. Slides were incubated with rabbit anti-chicken IgG (Jackson Immuno Labs, 303–005-003) and anti-rabbit HRP (Roche, 05269679001) followed by Venetana DAB detection kit (Roche, 05266645001) to visualize V5 and TDP-43 positive areas, or Discovery Purple kit to visualize pTDP-43 (Roche, 07053983001). Slides were counterstained with hematoxylin (Roche, 05266726001) and bluing reagent (Roche, 05266769001). Image acquisition was performed with the Panoramic P250 (3DHistech) scanner under 20X magnification. ChAT positive motor neurons were quantified using Visiopharm Version 2023.06 with a custom AI-based algorithm trained to detect motor neurons within the ventral horn. Total number of motor neurons calculated by the algorithm was divided by the total number of ventral horns to get the average number of motor neurons per ventral horn.

Wholemount NMJ staining and image analysis

Gastrocnemius (GA) and Tibialis anterior (TA) muscles were dissected and fixed in freshly prepared 2% paraformaldehyde in phosphate buffered saline (PBS) for 4 h on ice and stored in PBS. Samples were transferred to a blocking and permeabilizing solution of 5% normal goat serum and 0.5% Triton X-100 in PBS for 1 h before pressed between two glass slides using binder clips for 30 min-1 h, after which the samples were returned to the blocking and permeabilizing solution for 30 min. The samples were then incubated overnight at 4 °C on a shaker with 1:1000 dilutions of anti-neurofilament (DSHB, 2H3) and 1:400 dilution of anti-synaptophysin (Cell Signaling, 36,406) primary antibodies in blocking and permeabilizing solution. After three washes in PBS with 0.5% Triton X-100, the samples were transferred to blocking and permeabilizing solution with 1:1000 dilution of Alexa fluor 488 plus goat anti-mouse IgG (Invitrogen, A32723), Alexa fluor 647 plus goat anti-rabbit IgG (Invitrogen, A32733), α-bungarotoxin conjugated Alexa Fluor 555 (Invitrogen, B35451), and 1:5000 dilution of cell mask blue (Invitrogen, H32720). After overnight incubation at 4 °C, samples were washed with 0.5% Triton X-100 in PBS followed by 30 min with water and mounted with Vectashield Vibrance hard mounting media (Vector labs, H-1700). The Perkin Elmer Phenix with Harmony high-content analysis software was used for image acquisition and analysis. Images were analyzed using Visiopharm Version 2023.06 using custom designed AI-based algorithm to assess myofiber area.

Cortical thickness measurement

Cortical thickness was measured from the edge of the brain section to the cingulum bundle in the motor cortex using SlideViewer software (3DHistech).

Western blots

Approximately 20 to 25 mg of tissue powder was homogenized in NP-40 lysis buffer with protease inhibitor (cOmplete, Roche, 4,693,124,001) and phosphatase inhibitor (phosSTOP, Roche, 4,906,837,001) to collect soluble fraction. Insoluble protein fractions were collected in an urea-SDS buffer. Lysates were suspended in loading buffer (LDS sample buffer (NuPAGE, NP0007) and sample reducing agent (NuPAGE, NP0004)). The samples were then heated at 75 °C for 15–30 min.Samples were loaded into the NuPage Bis–Tris 4–12% Midi gel (WG1403BOX) with Bolt MES SDS running buffer (Invitrogen, B0002) and transferred to PVDF membrane (Invitrogen, IB24001) or nitrocellulose membrane (Invitrogen, IB23001) using iBlot 2 Gel Transfer Device (Invitrogen, IB21001). Membraneswere probed with primary antibodies overnight at 4 °C and then probed with IRDye IgG Secondary Antibody (LI-COR) for visulaization. Blots were scanned on an Odyssey® CLx scanner (LI-COR, 9140) for target protein image capture. Rever 700 Total Protein Stain (LI-COR, 926–11,011) was used for protein normalization according to manufacturer's directions. Image acquisition and band intensity quantification were done by the Image Studio Software (LI-COR).The source of primary antibodies and dilutions were as follows: V5-Tag (E9H8O) (Cell Signaling Technology, 80076S, 1:1,000), Profilin 1 (Sigma, P7749, 1:1,000), phospho-TDP-43 (Proteintech, 80,007–1-RR, 1:500), TDP-43 (Proteintech, 12,892–1-AP, 1:1000; 10,782–2-AP, 1:1,000; 18,280–1-AP, 1:1,000), TDP-43 C-terminal (Sigma, T1580) pTDP-43 (Proteintech, 80,007–1-RR, 1:500), mouse anti-GAPDH (Cell Signaling Technology, 97166S, 1:1000), rabbit anti GAPDH antibody (Cell Signaling Technology, 2118, 1:1000), humanized ATXN2 (Biogen, 1F9, 1ug/mL), mouse anti ATXN2 (BD biosciences, 611,378, 1:500). The source of secondary antibodies and dilutions were as follows: IRDye 800CW goat anti rabbit (LI-COR, 92,632,211, 1:10,000), IRDye 680CW goat anti mouse (LI-COR, 92,668,070, 1:10,000), IRDye 800CW goat anti mouse (LI-COR, 92,632,210, 1:10,000), IRDye 680CW goat anti rabbit (LI-COR, 92,668,071, 1:10,000), IRDye® 680RD Goat anti human (LI-COR, 92,668,078, 1:10,000). The primary and secondary antibodies were diluted with Intercept protein-free antibody diluent.

RNA purification and analysis

RNA was isolated from 15 to 20 mg of mouse tissue powder using the Qiagen miRNeasy Mini kit (Qiagen, 217,004) and the fully automated QIAcube Connect according to the manufacturer's guidelines. Produced cDNA using the High-Capacity cDNA RT Kit (ThermoFisher Scientific, 4,388,814) according to manufacturer's protocol. Quantitative real-time PCR (RT-qPCR) was performed using TaqMan Gene Expression Assays for Atxn2 (Mm00485946_m1) and Tbp (Mm01277042_m1) and the QuantStudio system (Life Technologies). Custom TaqMan Small RNA Assays (ThermoFisher Scientific) were generated to target the sense strand of the artificial miRNA.

Transcriptional analysis of immune response and neuroinflammation

RNA sequencing libraries were generated using the Kapa mRNA HyperPrep Kit (Roche, #KK8581). Libraries were sequenced on a NovaSeq 6000 in paired-end mode, 2×100 bp, generating 106 million mapped pairs in average. Fastq files were generated from bcl files using bcl2fastq v2.20 (Illumina). Alignment of reads was done with STAR version 2.7.2d against the mouse genome version GRCm38 with GENECODE annotation version M25 [35, 36]. The human PFN1 gene from reference genome GRCh38, GENCODE version v34, as well as the custom-built sequence of the AAV vector were added to the mouse genome as artificial chromosomes. Gene expression quantification was carried out using RSEM version 1.3.2 [37]. Differential expression analysis was done using the Quickomics pipeline that employed DESeq2 version 1.34.0 [38, 39].

Weighted gene co-expression network analysis (WGCNA)

Co-expression networks using WGCNA for Target ALS and PFN1-C71G mouse datasets were generated to identify modules of highly co-expressed groups of genes. WGCNA uses a topological overlap-based dissimilarity as input to average-linkage hierarchical clustering that results in a dendrogram. The normalized the raw counts data by variance stabilizing transformation (VST) in DESeq2 is used as the input data in WGCNA. Modules are identified as branches in the dendrogram using Dynamic Tree Cut. We used weighted correlation with individual sample weights determined as described above and the "signed hybrid" network in which positively correlated genes are considered connected. In analyses of people with ALS and mouse data we used merging heights of 0.3 for main modules. The module merging height equals 1-the threshold correlation that module eigengenes above which modules are merged.

Finally, we performed module preservation analysis, using modulePreservation function in WGCNA, to evaluate whether the gene co-expression network identified in PFN1 mouse is preserved in Target ALS C9 and SOD1 ALS human datasets, respectively. The module with Zsum score smaller than 2 is considered as not preserved, the Zsum score between 2 to 10 is considered as moderately preserved and the Zsum score greater than 10 is the strong preserved module.

Statistical analysis

Statistical significance was measured using GraphPad Prism 9.0.0 software (GraphPad Software, San Diego, CA). Motor behavior (grip strength, open field, rotarod) and body weight data were excluded from animals that dropped out of the study due to non-disease phenotype related deaths (fighting injury-related euthanasia, tumor development) and those with signs of foot and leg-injuries from fighting were excluded from dual lever muscle force measurements (WT vehicle: n = 3; PFN1 vehicle: n = 4, PFN1 amiR-Atxn2: n = 1). The two-way mixed-model ANOVA with Sidak or Tukey's multiple comparisons test was used to compare the mean of each group with every other group. For the pathology quantification, Student's t-test were performed. For the qPCR and Western blot experiments, one-way ANOVA with Tukey's or Dunnett's multiple comparisons test or Student's t-test were performed. Data were expressed as mean ± standard error of the mean (SEM). Data were judged to be statistically significant when $P < 0.05$.

Supplementary Information

The online version contains supplementary material available at https://doi.org/10.1186/s40478-025-02005-z.

Supplementary material 1

Supplementary material 2

Acknowledgements

The authors would like to acknowledge David Koske for providing assistance with CMAP recordings, and Galina Marsh for immunohistochemistry assistance. We are indebted to Paulo Loos for his contributions to the NMJ imaging and automated analysis.

Author contributions

Z.C.E.H and D.Y.K. designed the experiments. Z.C.E.H., X.L., D.B., Y.G., Y.I., D.F., A.S., R.D., I.I., A.G., and Y.L. performed the experiments. S-C.L. advised on AAV vector and dose. Z.C.E.H., X.L., D.B., Y.G., A.S., R.D., H.M.A., T.C., and D.Y.K. analyzed experimental data. Z.C.E.H, M.Z., S.C., and D.H. performed analyses on RNAseq data. L.J. designed programs for automated analysis of immunohistochemical images. S.B., A.U., S.D., and E.G. designed and produced AAV-amiR-ATXN2. D.Y.K. supervised all work and Z.C.E.H and D.Y.K. wrote the manuscript. All authors reviewed and approved the final version of the manuscript.

Funding

This study was sponsored by Biogen (Cambridge, MA, USA). All funding was provided by Biogen.

Data availability

Raw RNA-seq data for mouse (GSE297399) and Target ALS (GSE153960) can be accessed via the National Center for Biotechnology Information's Gene Expression Omnibus database. UMiami RNA-seq dataset is currently under review but can be made available upon reasonable request. All other data can be made available upon reasonable request.

Declarations

Ethical approval and consent to participate

All procedures were formed in accordance with NIH Guide for the Care and Use of Experimental Animals and studies were approved by the Biogen Institutional Animal Care and Use Committee (IACUC).

Consent for publication

Not applicable.

Competing interests

All authors are employees of Biogen (Cambridge, MA, USA).

Received: 24 December 2024 Accepted: 11 April 2025

References

1. Oskarsson B, Gendron TF, Staff NP (2018) Amyotrophic lateral sclerosis: an update for 2018. Mayo Clin Proc 93:1617–1628
2. Neumann M et al (2009) Phosphorylation of S409/410 of TDP-43 is a consistent feature in all sporadic and familial forms of TDP-43 proteinopathies. Acta Neuropathol 117:137–149
3. Klim JR et al (2019) ALS-implicated protein TDP-43 sustains levels of STMN2, a mediator of motor neuron growth and repair. Nat Neurosci 22:167–179
4. Barmada SJ et al (2010) Cytoplasmic mislocalization of TDP-43 is toxic to neurons and enhanced by a mutation associated with familial amyotrophic lateral sclerosis. J Neurosci 30:639–649
5. Kabashi E et al (2010) Gain and loss of function of ALS-related mutations of TARDBP (TDP-43) cause motor deficits in vivo. Hum Mol Genet 19:671–683
6. Baughn MW et al (2023) Mechanism of STMN2 cryptic splice-polyadenylation and its correction for TDP-43 proteinopathies. Science 379:1140–1149
7. Brown AL et al (2022) TDP-43 loss and ALS-risk SNPs drive mis-splicing and depletion of UNC13A. Nature 603:131–137
8. Ma XR et al (2022) TDP-43 represses cryptic exon inclusion in the FTD-ALS gene UNC13A. Nature 603:124–130
9. Wils H et al (2010) TDP-43 transgenic mice develop spastic paralysis and neuronal inclusions characteristic of ALS and frontotemporal lobar degeneration. Proc Natl Acad Sci USA 107:3858–3863
10. Becker LA et al (2017) Therapeutic reduction of ataxin-2 extends lifespan and reduces pathology in TDP-43 mice. Nature 544:367–371
11. Elden AC et al (2010) Ataxin-2 intermediate-length polyglutamine expansions are associated with increased risk for ALS. Nature 466:1069–1075
12. Sproviero W et al (2017) ATXN2 trinucleotide repeat length correlates with risk of ALS. Neurobiol Aging 51:178.e1-178.e9
13. Zeballos CM et al (2023) Mitigating a TDP-43 proteinopathy by targeting ataxin-2 using RNA-targeting CRISPR effector proteins. Nat Commun 14:6492
14. Carmen-Orozco RP et al (2024) Elevated nuclear TDP-43 induces constitutive exon skipping. Mol Neurodegener 19:45
15. Nejedla M et al (2016) Profilin connects actin assembly with microtubule dynamics. Mol Biol Cell 27:2381–2393
16. Schmidt EJ et al (2021) ALS-linked PFN1 variants exhibit loss and gain of functions in the context of formin-induced actin polymerization. Proc Natl Acad Sci USA. https://doi.org/10.1073/pnas.2024605118
17. Henty-Ridilla JL, Juanes MA, Goode BL (2017) Profilin directly promotes microtubule growth through residues mutated in amyotrophic lateral sclerosis. Curr Biol 27:e3534
18. Matsukawa K et al (2016) Familial amyotrophic lateral sclerosis-linked mutations in profilin 1 exacerbate TDP-43-induced degeneration in the retina of drosophila melanogaster through an increase in the cytoplasmic localization of TDP-43. J Biol Chem 291:23464–23476
19. Wu CH et al (2012) Mutations in the profilin 1 gene cause familial amyotrophic lateral sclerosis. Nature 488:499–503
20. Tanaka Y, Nonaka T, Suzuki G, Kametani F, Hasegawa M (2016) Gain-of-function profilin 1 mutations linked to familial amyotrophic lateral sclerosis cause seed-dependent intracellular TDP-43 aggregation. Hum Mol Genet 25:1420–1433
21. Smith BN et al (2015) Novel mutations support a role for profilin 1 in the pathogenesis of ALS. Neurobiol Aging 36(1602):e1617-1627
22. Yang C et al (2016) Mutant PFN1 causes ALS phenotypes and progressive motor neuron degeneration in mice by a gain of toxicity. Proc Natl Acad Sci USA 113:E6209–E6218
23. Grassano M et al (2024) Sex differences in amyotrophic lateral sclerosis survival and progression: a multidimensional analysis. Ann Neurol 96:159–169
24. Hawley ZCE et al (2025) Dorsal root ganglion toxicity after AAV intra-CSF delivery of a RNAi expression construct into non-human primates and mice. Mol Therapy 33:215–234
25. McCombe PA et al (2015) Serial measurements of phosphorylated neurofilament-heavy in the serum of subjects with amyotrophic lateral sclerosis. J Neurol Sci 353:122–129
26. Ziff OJ et al (2023) Integrated transcriptome landscape of ALS identifies genome instability linked to TDP-43 pathology. Nat Commun 14:2176
27. Humphrey J et al (2023) Integrative transcriptomic analysis of the amyotrophic lateral sclerosis spinal cord implicates glial activation and suggests new risk genes. Nat Neurosci 26:150–162
28. Canet-Pons J et al (2021) Atxn2-CAG100-KnockIn mouse spinal cord shows progressive TDP43 pathology associated with cholesterol biosynthesis suppression. Neurobiol Dis 152:105289
29. Tian Y et al (2021) Tau-tubulin kinase 1 phosphorylates TDP-43 at disease-relevant sites and exacerbates TDP-43 pathology. Neurobiol Dis 161:105548
30. Nourse JB Jr et al (2023) Integrated regulation of dopaminergic and epigenetic effectors of neuroprotection in Parkinson's disease models. Proc Natl Acad Sci USA 120:e2210712120
31. Suk TR, Rousseaux MWC (2020) The role of TDP-43 mislocalization in amyotrophic lateral sclerosis. Mol Neurodegener 15:45
32. Walker AK et al (2015) Functional recovery in new mouse models of ALS/FTLD after clearance of pathological cytoplasmic TDP-43. Acta Neuropathol 130:643–660
33. Fil D et al (2016) Mutant profilin1 transgenic mice recapitulate cardinal features of motor neuron disease. Hum Mol Genet. https://doi.org/10.1093/hmg/ddw429
34. Huang Z et al (2020) Inhibition of IL-6/JAK/STAT3 pathway rescues denervation-induced skeletal muscle atrophy. Ann Transl Med 8:16821
35. Frankish A et al (2019) GENCODE reference annotation for the human and mouse genomes. Nucleic Acids Res 47:D766–D773
36. Dobin A, Gingeras TR (2016) Optimizing RNA-seq mapping with STAR. Methods Mol Biol 1415:245–262
37. Li B, Dewey CN (2011) RSEM: accurate transcript quantification from RNA-seq data with or without a reference genome. BMC Bioinformatics 12:323
38. Gao B et al (2021) Quickomics: exploring omics data in an intuitive, interactive and informative manner. Bioinformatics 37:3670–3672
39. Love MI, Huber W, Anders S (2014) Moderated estimation of fold change and dispersion for RNA-seq data with DESeq2. Genome Biol 15:550

Publisher's Note